

## 4.2.5.2 Forcing Functions

### 4.2.5.2.1 Excitation Resulting from Random Turbulence

The experimentally derived forcing functions are reduced to a non-dimensional form so that scaling to reactor conditions (scale and temperature) is achievable. The dynamic similitude of the forcing function and the RV internals is created between the 1/8 scale model and the full scale model by using the Strouhal number.

The non-dimensional PSD( $S_t$ ) and the correlation lengths reported in Section 4.2.2.4 are created as a function of the Strouhal number whose definition is based upon the hydraulic diameter of the downcomer for the mockup. This non-dimensional PSD( $S_t$ ) is then converted to a dimensional pressure PSD( $f$ ) using the relationship of the hydraulic diameter and velocity with the Strouhal number to create the dynamic similitude between the 1/8 scale and the full scale numerical models. Similarly, the dynamic similitude for correlation length is retained based upon the relationship of the hydraulic diameter and velocity with the Strouhal number for the two numerical models. Provided the mean velocity in the downcomer ( [ ] ft/sec) is maintained between the HYDRAVIB flow test and the full scale design, then the dynamic similitude between the 1/8 scale and the full scale analysis is preserved for the forcing function.

The validity of the transposition is sustained by the comparison of the Reynolds number for the flow conditions between the mockup and reactor. The Reynolds numbers are:

$$Re \sim [ ] \text{ (for mockup conditions).}$$

$$Re \sim [ ] \text{ (for reactor, hot shutdown conditions).}$$

Because both values are higher than  $2 \times 10^5$ , fully developed turbulent flow conditions exist in both cases. The formulas for the turbulent forcing functions derived for 1/8 scale HYDRAVIB tests and developed in Section 4.2.2.4 have dynamic similitude with the full scale model and can be used in the full scale analysis of the hot standby reactor condition.

### 4.2.5.2.2 Excitation Resulting from Acoustic Pressure Fluctuations

#### RCP Acoustic Pressure Fluctuations

The numerical simulation of the full scale RV internals does not explicitly consider the excitation resulting from the narrow band acoustic pressure fluctuations generated by the RCP. These acoustic pressure waves are estimated to be approximately [ ] (0-peak) and are associated with the RCP blade passing frequency ([ ]). Because a large degree of separation exists between this blade passing frequency and the significant frequencies of the beam mode of the CB ( $\sim$ [ ] Hz, modes [ ] with loaded core) and the plate mode of the LSP ( $\sim$ [ ] Hz, mode [ ] with loaded core), it is not possible for this narrow band acoustic pressure fluctuation to create significant excitation of the RV lower internals. Therefore,

neglecting these pressure fluctuations in the model of the RV lower internals is acceptable. The magnitude and influence of the RCP acoustic pressure fluctuations on the RV lower internals are measured during the HFT of the U.S. EPR to confirm this conclusion.

### Loop Acoustics

The acoustic pressure fluctuations associated with flow loop acoustics are created by minute changes in the momentum of the primary fluid as it enters the downcomer cavity of the RPV. Loop acoustics have the characteristics of a uniform pressure field with low frequency and high amplitude that are produced by a global response of the loops rather than locally produced turbulence. Loop acoustics are generally associated with the slight imbalance of flow rates of RCS primary pumps, with a time constant of tenths of a second or more. Being uniform, the homogeneous pressure field in the downcomer has virtually no effect on the response of the RPV internals since there is no asymmetrical loading and excitation imparted to the CB beam mode which dominates the response of the lower internals. Consequently, no attempt is made to accurately measure or model this low frequency contribution.

### Acoustic Resonance

A screening methodology is incorporated into the design of the RCS piping system and piping systems attached to the RCS components (i.e., RV, RSGs, Prez) to preclude the possibility of potentially damaging effects to the internal structures of these components occurring from acoustic resonance caused by shear wave resonance of valve stand pipes (i.e., dead leg of closed relief valve). The screening methodology is based on design criterion which utilizes the relationship among the Strouhal number, the Mach number, and the stand pipe dimensions to effectively eliminate the acoustic resonance excitation in the RCS piping design and the piping systems attached to the RCS for the plant operating conditions at the power levels. This eliminates the need for an analytical evaluation of acoustic resonance. See Appendix A.2.1 for details regarding the screening methodology.

### **4.2.5.3 Modal Damping**

Unlike the forcing function, the modal damping ratio values obtained with the mockup are not necessarily representative of the reactor conditions. Therefore, using the following dedicated analysis, an appropriate damping value is determined for the modes that are representative of the full scale model.

#### **4.2.5.3.1 Structural Damping (all modes)**

Because the structure is expected to be functioning in nominal conditions (i.e., very low amplitudes vibrations), the structural damping ( $\zeta_{\text{structural}}$ ) is primarily governed by material and slip damping, which can not be estimated through predictive analysis. A conventional or typical value of [ ] percent of critical damping is used.

#### 4.2.5.3.2 Fluid Damping for Core Barrel Beam-type Modes

Fluid damping arises from different phenomena:

- Radiation damping:  $\zeta_{\text{radiation}}$
- Viscous damping:  $\zeta_{\text{viscous}}$
- Added damping due to turbulent flow:  $\zeta_{\text{flow}}$

Radiation damping is important for structures immersed in a relatively heavy fluid and vibrating at medium or high frequencies and does not apply to the CB. No attempt is made to account for radiation damping.

The added damping due to viscous dissipation of the motion of a cylinder in a fluid-filled annulus is estimated using the following approximate expression, which is valid for vibration amplitudes much less than one diameter (Reference 2, Equation 8-13).

$$\zeta_{\text{viscous}} = \frac{\pi}{2} \frac{\rho D^2}{m + M_h} \left( \frac{\nu}{\pi D^2} \right)^{1/2} \left( \frac{1 + (D/D_o)^3}{[1 - (D/D_o)^3]^2} \right)$$

Where:

- D = Inner cylinder diameter.
- D<sub>o</sub> = Outer cylinder diameter.
- ρ = Fluid density.
- ν = Fluid kinematic viscosity.
- f = Natural frequency.
- M = Cylinder mass per unit length.
- M<sub>h</sub> = Hydrodynamic added mass per unit length.

Using this equation, viscous damping values ranging from less than [ ] modal damping (in cold conditions) to about [ ] (in hot conditions) are obtained, primarily due to the reduction in the kinematic viscosity of the fluid. This is consistent with the increase in modal damping values obtained during mockup tests when switching from a dry to a wet configuration. Consequently, viscous damping in reactor hot conditions is [ ]

The additional damping created from the turbulent fluid flow is determined from the following expression for parallel flow, which is valid for fluid flow having a high Reynolds number that is parallel to the axis of an elastic cylinder (Reference 2, Equation 8-25).

$$\zeta_{\text{flow}} = \frac{1}{8\pi} C_N C_I \frac{U}{f_n D} \frac{\rho D^2}{m}$$

Where:

$C_N$  = Friction coefficient.

$C_I$  = Added mass coefficient.

These two coefficients are extrapolated from the HYDRAVIB mockup data. Because a similitude of the downcomer velocity is maintained between the mockup and the full scale prototype, the non-dimensional terms are canceled and only fluid density is corrected:

$$\left[ \right]$$

The added damping due to turbulent flow is estimated as follows:

$$\zeta_{\text{still\_water}} = [ \quad ] \text{ (from "phase 2 of the HYDRAVIB tests)}$$

$$\zeta_{\text{flow}} = [ \quad ] \text{ (Section 4.2.3)}$$

Hence,

$$\zeta_{\text{flow\_mockup}} = [ \quad ]$$

Using the following values of density for water at 68°F and 578°F;

$$\rho_{\text{mockup\_conditions}} = 62.303 \text{ lbm/ft}^3.$$

$$\rho_{\text{reactor\_conditions}} = 45.385 \text{ lbm/ft}^3$$

The added damping due to fluid flow is therefore estimated to be equal to:

$$\zeta_{\text{flow\_reactor}} = [ \quad ]$$

Finally, the total damping value applied to the CB beam modes is equal to:

$$\zeta_{\text{reactor}} = [ \quad ]$$

$$\zeta_{\text{reactor}} = [ \quad ]$$

Except for the neglected viscous damping at about [ ] the  $\zeta_{\text{reactor}}$  of [ ] is a best-estimate value.

#### 4.2.5.3.3 Fluid Damping for Heavy Reflector Beam-type Modes

The HR-CB fluid annulus exhibits a small width to radius ratio ( [ ] ). A high hydrodynamic mass and low natural frequencies are created by these conditions. Consequently:

- Acoustic radiation damping is negligible.
- Viscous damping is expected to be the primary contributor.

The added damping due to viscous effects is calculated by the same method that is used for the RV downcomer annulus:

$$\zeta_{\text{viscous}} = \frac{\pi}{2} \frac{\rho D^2}{m + M_h} \left( \frac{v}{\pi D^2} \right)^{1/2} \left( \frac{1 + (D/D_o)^3}{[1 - (D/D_o)^3]^2} \right)$$

This yields a modal damping ratio of about [ ] Flow-induced damping is not accounted for in this value, although a non-zero fluid-flow exists in the HR-CB annulus. The mean flow velocity value of [ ] ft/s exists, which when considered with a mean radial hot gap value of [ ] inch yields a relatively high Reynolds number ( $Re \sim [ ]$  ). The actual flow damping is significantly higher than that applied in the analysis.

#### 4.2.5.3.4 Fluid Damping for Shell-type Modes

The other shell-type modes involve the coupled flexural motion of both the CB and HR. The radiation damping effects are neglected for the shell modes because in the frequency range of interest, acoustic and bending wavelengths differ by orders of magnitude and radiation efficiency is expected to be low.

For an estimation of the added modal damping ratio due to viscous effects, the following expression was derived by R.J Gibert (Reference 3, Equation 15.17):

$$\zeta_{\text{viscous}} = \frac{1}{2} \sqrt{\frac{v}{2\omega_o e^2}}$$

Where:

$v$  = kinematic viscosity.

$e$  = one-half the HR/CB gap width.

This expression is based on the ratio of viscous (dissipation) to mass (reactance) terms of the net force by unit area for a plate or shell. It is valid provided the bending wavelength remains longer than the plate or fluid thickness, which is the case for the CB and HR fluid annulus as shown below.

Using the following numerical values at hot condition:

$$\nu = [ \quad ] \text{ in}^2/\text{sec.}$$

$$e = [ \quad ] \text{ inch.}$$

The added modal damping due to viscous effects for shell modes is estimated as:

$$\left[ \quad \quad \quad \right]$$

Numerically, this creates additional damping ranging from [  $\quad$  ] to [  $\quad$  ] in the frequency band spanning from [  $\quad$  ] to [  $\quad$  ] Hz.

#### 4.2.5.3.5 Summary of Modal Damping Values

The previously obtained modal damping ratios are summarized in Table 4-7 for the modes in the 0 to 12.5 Hz frequency band.

**Table 4-7—Summary of Modal Damping Ratios used for FIV Estimation**

A large, empty rectangular frame with a thick black border, centered on the page. It is intended to contain the data for Table 4-7, but the content is missing.

## 4.2.6 FIV Acceptance Criteria for the RV Lower Internals

The acceptance criteria established in this section are imposed upon the results for the numerical simulations but are also applicable to the experimental results obtained during HFT.

### 4.2.6.1 Acceptance Criteria for Displacements

The displacement limits imposed upon the RV lower internals are based on preventing impacts with the adjacent structures. Close proximity exists between the following structures:

- Between the CB and the Radial Guides attached to the RV ID.
- Between the CB with the UCP.
- Between the HR and the CB.

Regarding the first and second bullets, the numerical simulation of the RV lower internals is a linear frequency domain analysis where the potential interaction between the CB and the radial guides at the LSP elevation and the CB and the UCP is assumed not to occur, which is verified with the theoretical results. The acceptance criteria for the vibration amplitudes between these components are based on the gap clearance between the adjacent structures because the interfacing structure has a static response.

For the third bullet, the acceptance criterion for vibration amplitudes between the HR and the CB is based on the  $\frac{1}{2}$  gap clearance between the adjacent structures. The radial gap clearance between HR and CB is reduced by a factor of two to ensure that vibration amplitudes for each of the two components does not result in impacts of the components.

Because the displacement response to turbulence, computed in units of (inch, rms), is based on a probability of excursions, the radial gap clearance is divided by a factor of 5 or 5 sigma, which is representative of approximately a 100 percent probability that this allowable displacement will not be exceeded, or that these structures will not interact with each other during full power operating conditions.

Applying the above criteria, the displacement limits for the RV lower internals are computed and reported in Table 4-8.

### 4.2.6.2 Acceptance Criteria for High Cycle Fatigue

The responses of the structures are computed in statistical units of measurement (e.g., the stress in units of psi, rms). A statistical analysis technique is used to develop an RMS fatigue curve from the ASME fatigue curve for austenitic steel, which is based on tests performed with sinusoidal loads. The full details of this technique are described in Reference 4, Chapter 11.

These curves are derived from the corresponding fatigue curves based on long-duration tests with deterministic loads, as published in the ASME Section III Boiler & Pressure Vessel Code.

The RMS fatigue curves are derived using the fatigue curves "A, B, & C" for the fatigue life

calculations for the FIV analysis of high cycle fatigue loadings. The RMS fatigue curve is provided in Figure 4-21.

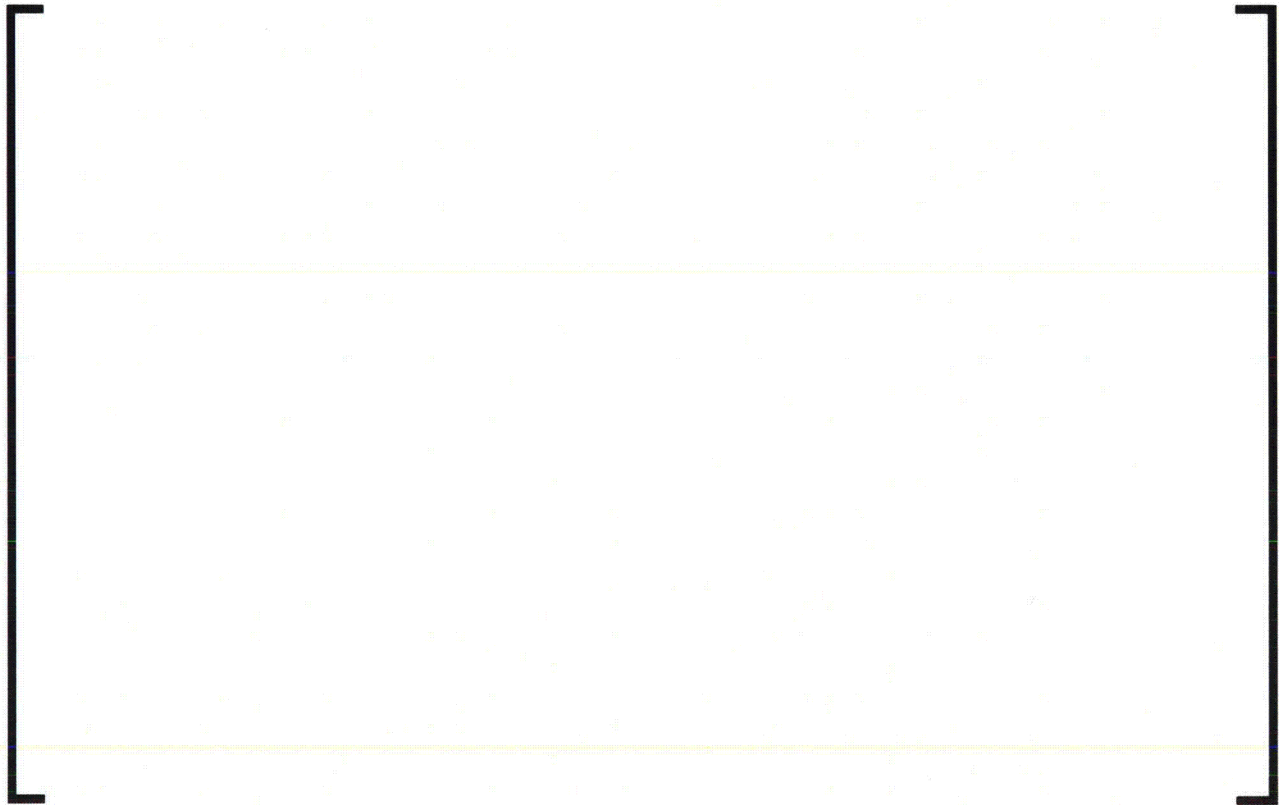
The primary plus secondary stress range ( $P_L + P_B + Q$ ) for the Level A & B service limits have not been determined. When these stresses are computed, the primary plus secondary stress range in the CB, for which the alternating flow-induced vibration (FIV) stress is cyclic, is expected to be less than 27.2 ksi. For the fatigue evaluation of a stress location within three wall thicknesses of a weld with the primary plus secondary stress range less than 27.2 ksi, the use of fatigue curve "B" is justified. When the primary plus secondary stress range exceeds 27.2 ksi, fatigue curve "C" is recommended. The allowable stress for fatigue curve "B" is [       ] psi, rms at  $10^{13}$  cycles. However, as a conservative approach, fatigue curve "C" is used for the acceptance criteria. The allowable stress for fatigue curve "C" is [       ] psi, rms at  $10^{13}$  cycles.

Recent NRC guidelines regarding the environmental effects upon the published ASME fatigue curves are provided in Reference 5. The fatigue curves published in the 2004 ASME Section III Appendices do not consider environmental effects. A review of Reference 5 confirms that the allowable stress and cycles of the fatigue curve do not change in the high cycle range of the curve (for cycles  $> 10^8$ ), which is the area of concern for most FIV analyses. However, to comply with Reference 5, it is necessary to consider an environmental correction factor ( $F_{en}$ ) in the fatigue analysis. Reference 5 refers to NUREG/CR-6909, Appendix A (Reference 6) for an acceptable method to determine the environmental correction factor for austenitic steels. According to Reference 6, Section A.2, the environmental correction factor is 1.0 if the strain ( $\epsilon$ ) is less than 0.10 percent, which is typically true of FIV analyses. Therefore, the environmental fatigue concerns identified in Reference 5 do not impact the FIV analysis of the RV lower internals.

**Table 4-8—FIV Displacement Limit for RV Core Barrel and Heavy Reflector**



**Figure 4-21—Fatigue Curves for Austenitic Steel Based on RMS Stress**



## 4.2.7 Response of the RV Lower Internals (Full Scale)

### 4.2.7.1 Full Power, Steady State, Normal Operating Conditions

The response of the RV lower internals to the turbulence in the downcomer and lower plenum is provided in this section for the HFT condition (Test #17) and the full power, steady state normal operating condition. The FIV results representative of the full power normal operating condition are determined from the analysis results for the HFT condition by using a scaling factor

( [       ] ) based on the ratio of the dynamic pressure term of the full power and HFT testing condition as discussed in Section 4.2.5. The results show that the RV lower internals meet the FIV acceptance criteria established in Section 4.2.6.

#### 4.2.7.1.1 Vibration Amplitudes

The amplitudes of vibration predicted for the U.S. EPR RV lower internals during HFT (Test #17) and the full power, steady state normal operating conditions are reported respectively in Table 4-9 and Table 4-10 and satisfy the acceptance criteria defined in Section 4.2.6.

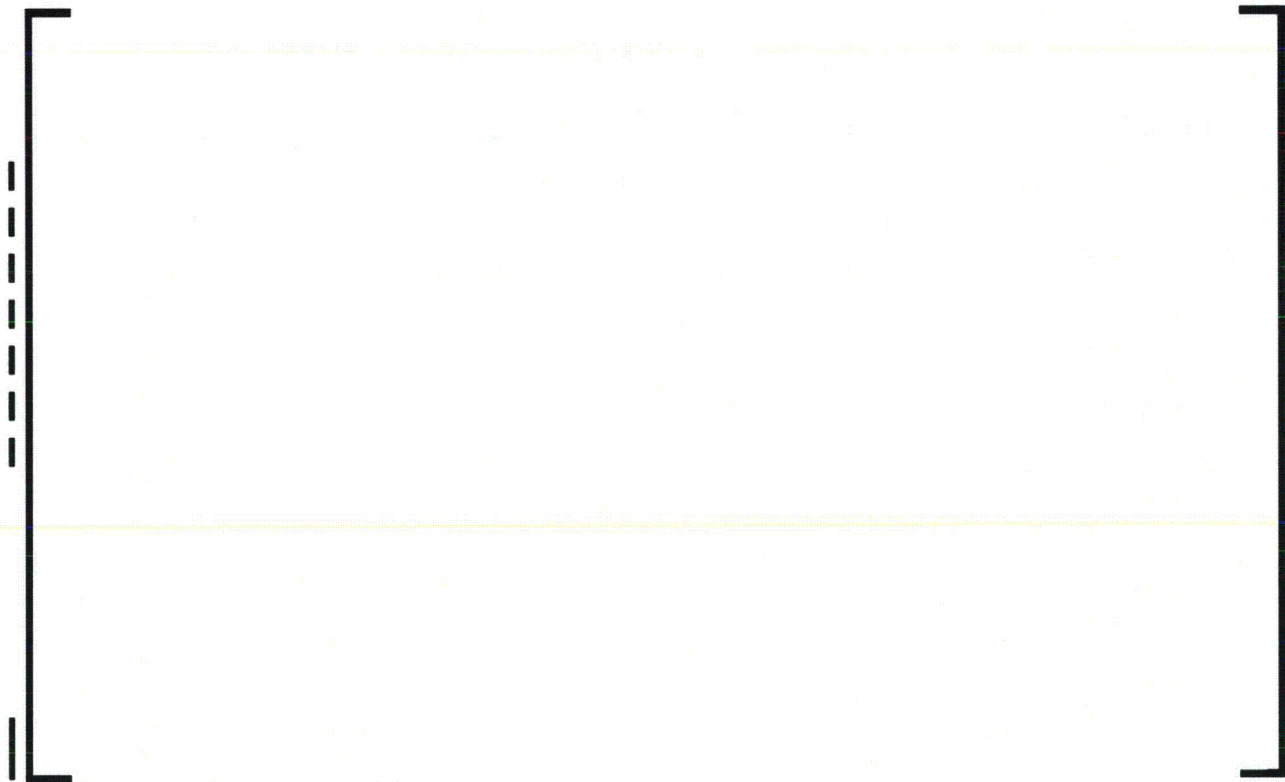
The corresponding frequency content is provided in Figure 4-23 and Figure 4-24. Mapping of the RMS displacement values is provided in Figure 4-25. These figures confirm that:



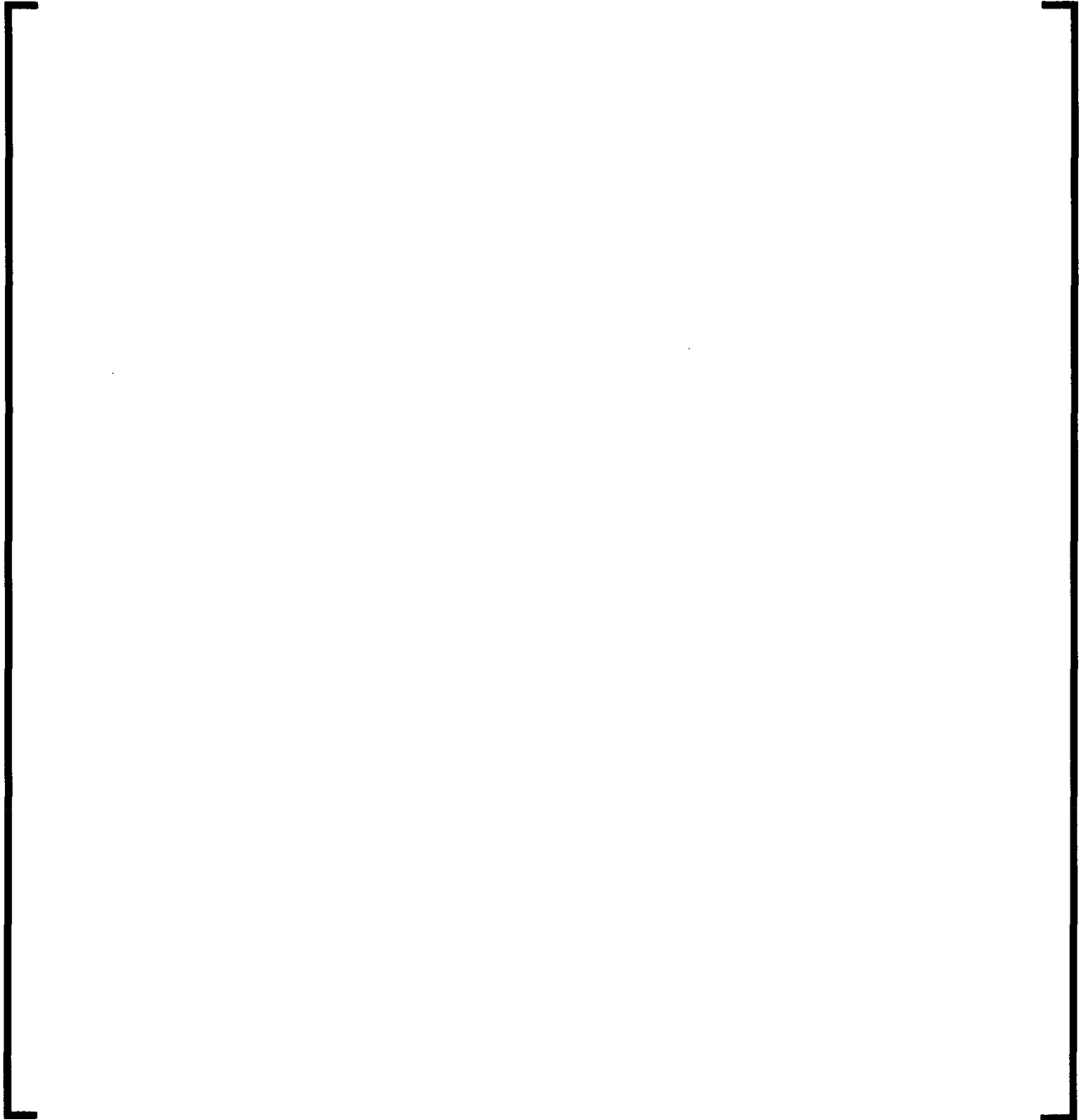
**Table 4-9—Displacement Response of the RV Internals (HFT #17)**

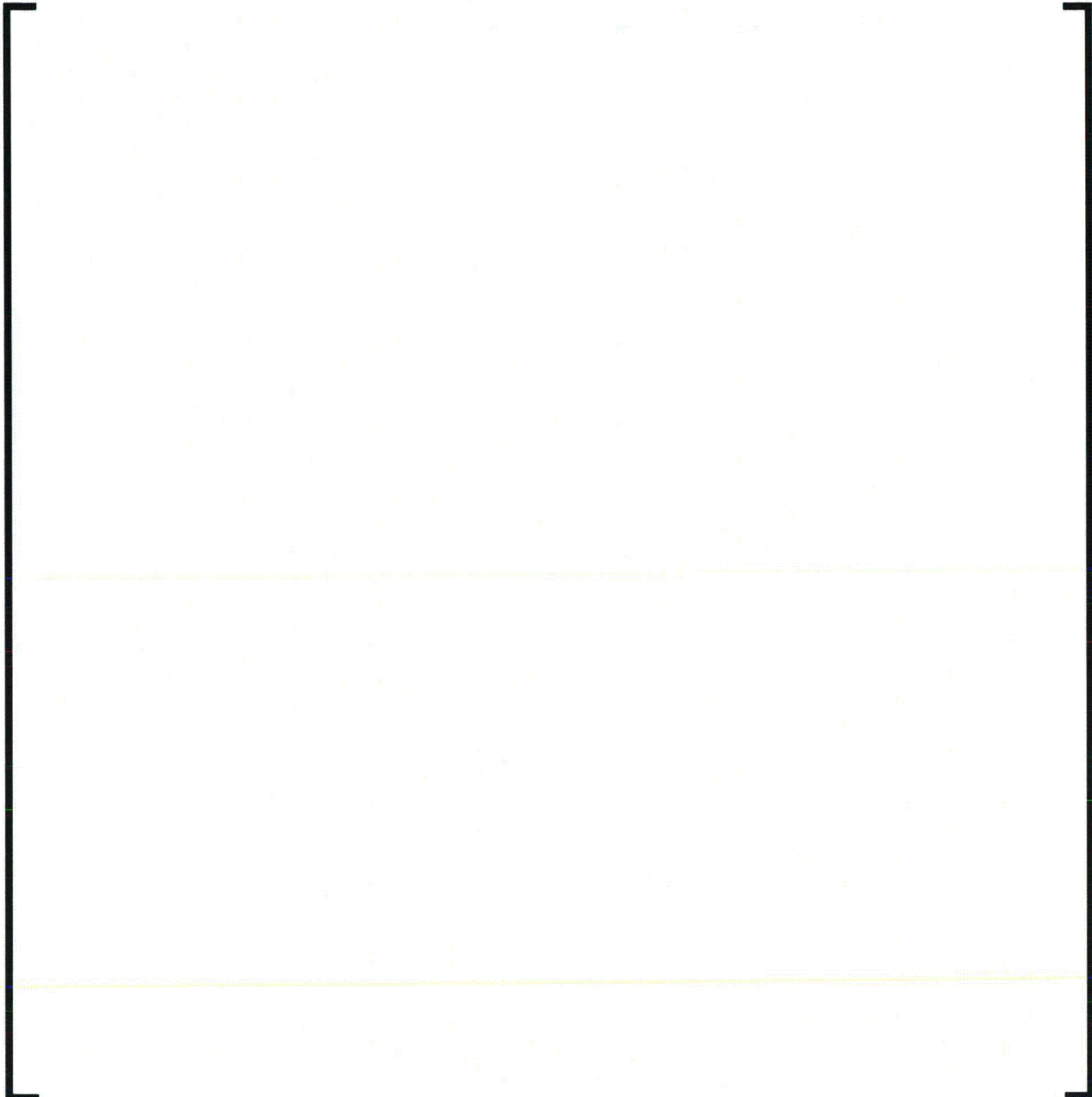


**Table 4-10—Displacement Response of the RV Internals (Full Power, Steady State Normal Operating Condition)**

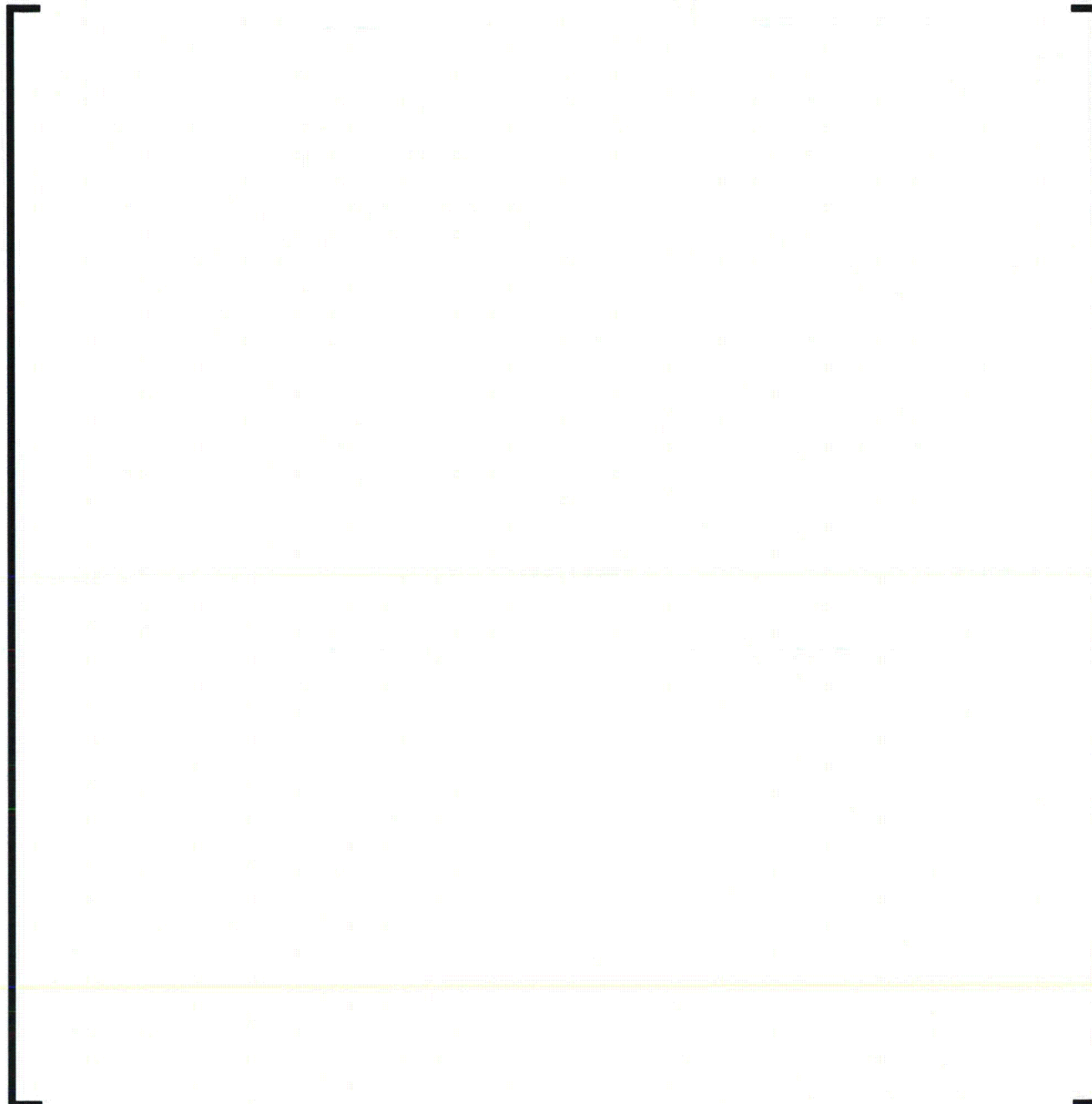


**Figure 4-22—RV Lower Internal Response Locations for Displacements**



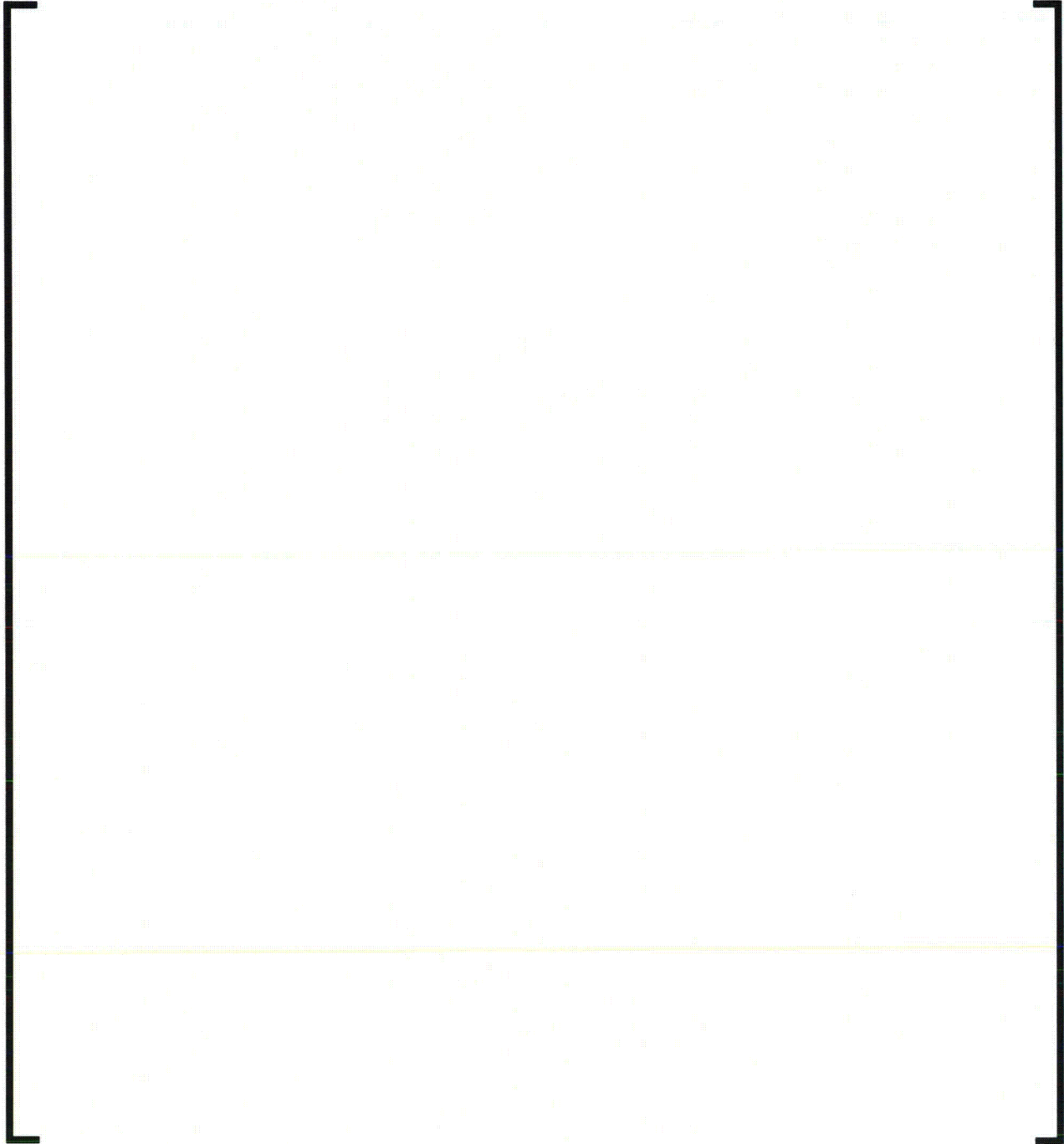
**Figure 4-23—RPSD and Corresponding Energy Distribution along  
Reactor 0° Axis****Notes for Figure 4-23:**

1. These graphical presentations are applicable to the HFT conditions of the U.S EPR RV lower internals. Multiplying the results by the square of the [ ] scaling factor, [ ] provides the solution for the full power steady state normal operating condition for the U.S. EPR RV lower internals.
2. See Figure 4-22 for the location of the RPSD on the RV lower internals.
3. Units (millimeter)<sup>2</sup>/Hz

**Figure 4-24—RPSD and Corresponding Energy Distribution along  
Reactor 90° Axis****Notes for Figure 4-24:**

1. These graphical presentations are applicable to the HFT conditions of the U.S EPR RV lower internals. Multiplying the results by the square of the [ ] scaling factor, [ ] provides the solution for the full power steady state normal operating condition for the U.S. EPR RV lower internals.
2. See Figure 4-22 for the location of the RPSD on the RV lower internals.
3. Units (millimeter)<sup>2</sup>/Hz

**Figure 4-25—Horizontal Displacements Levels Mapping for Reactor  
Conditions FIV Simulation**



Notes for Figure 4-25:

1. These graphical presentations are applicable to the HFT conditions of the U.S EPR RV lower internals. Multiplying the results by the [ ] scaling factor provides the solution for the full power steady state normal operating condition for the U.S. EPR RV lower internals.

#### 4.2.7.1.2 Stress Levels

The distribution of stress is displayed in Figure 4-26. As expected, peak stresses are located at the junction between the CB shell and the flange (local bending occurs in this region) with secondary stress concentrations in the vicinity of the nozzles.

A maximum stress of [ ] MPa, rms (or [ ] psi, rms) is shown in Figure 4-26 at the CB flange elevation. Applying a fatigue strength reduction factor (FSRF) of [ ] for the cylinder to flange juncture, a weld quality factor ( $f=1$ ) for dynamic loading dynamic as prescribed by ASME Section III, Table NG-3352-1 for the category C, Type I weld joint, and the scaling factor of [ ], a peak stress of approximately [ ] psi, rms is obtained for the full power normal operating condition.

To evaluate the RV lower internals for fatigue, the number of cycles per unit time is taken from the displacement results (See Table 4-10). Considering a crossing frequency of [ ] Hz and based upon 60 years of continuous operation (i.e., assuming a 100 percent capacity factor), this yields a number of cycles of about [ ]. Using Figure 4-21 and fatigue curve "C", the allowable number of cycles for the [ ] psi, rms peak stress is  $> 10^{13}$  cycles. Therefore the fatigue usage factor is less than [ ]. The endurance limit of approximately [ ] psi, rms at [ ] cycles is greater than four times the stress in the CB ( [ ] psi, rms). Therefore, high cycle fatigue failure resulting from the random turbulence in the RV downcomer is not predicted to occur.

**Figure 4-26—Axial Stress Distribution**



Notes for Figure 4-26:

1. These graphical presentations are applicable to the HFT conditions of the U.S EPR RV lower internals. Multiplying the results by the [ ] scaling factor provides the solution for the full power steady state normal operating condition for the U.S. EPR RV lower internals.

#### 4.2.7.1.3 Uncertainty and Bias in the Predicted Response

The structural model for the lower internal assembly evaluates the nominal (design) dimensions of the components to determine the natural frequencies and mode shapes of these components. As such, the analytical model does not specifically consider the manufactured tolerances associated with the geometry of the structures and the differences in material properties values established in the ASME code and the as-built values. Since the analytical results are compared to HFT results, the appropriate practice is to consider the "best estimate" design inputs in order to obtain the best agreement between the analytical and field test results. The implication of this approach is addressed in the following paragraph.

The fluid-structure coupling mechanism for random turbulence is weak in that the flow field induced by the structural motion is linearly superimposed on the incident flow field. In contrast, a strongly coupled fluid-structural system, which is characterized by large structural motion, will induce fluid velocities and completely distort the incident flow field. Vortex-shedding induced vibration and fluid-elastic instability of heat exchange tubes are examples of strongly coupled fluid-structure systems. With these strongly fluid-structural coupled systems, the sensitivity of the FIV mechanism to the natural frequencies of the components becomes fundamental as to whether or not this mechanism is active and to the strength of the response. For the weakly fluid-structure coupling associated with random turbulence, the relationship between the natural frequencies and the response of the structure is not as strongly associated; therefore, the slight variation in the natural frequencies that would be attributed to manufactured tolerances and material property variations does not significantly alter the forcing function and the response of the structure.

Nonetheless, a general assessment of the FE model accuracy based upon the uncertainties associated with various attributes of the analysis was undertaken to establish an overall range of uncertainty in the computed frequencies and the level of response. An overall summary of the range of uncertainties in the modal frequencies and response level of the RPVI is provided below. The assessment of the uncertainties associated with the analyses can be itemized into the following three categories:

- Uncertainties on structural compliance.
- Uncertainties on fluid forcing function.
- Combination of the above to assess the global uncertainty on the response levels.

#### Uncertainty on Structural Compliance

The uncertainty associated with the dynamic flexibility of the RPV lower internal assembly is assessed for:

- Restoring forces: linearity, discretization, boundary and interfaces conditions, material properties, and manufacturing tolerances effects.
- Damping forces: structural, viscous, and flow induced contributions.
- Inertia forces: structural, and hydro-dynamically induced.

### Uncertainty of the Forcing Function for Turbulence

The uncertainties on the forcing function for turbulence considers the following contributors:

- Uncertainties with the measurement of dynamic pressures.
- Uncertainties with the spectral parameters (slopes and frequencies).
- Uncertainties on reactor flow rates.

### Uncertainty of the Fundamental Frequency of the CB

As stated in Section 4.2.8, the response of the lower internals to random turbulence is primarily dominated by the fundamental beam mode of the CB. From Table 4-5, the best estimate value for the fundamental frequency of the CB beam modes are [ ] Hz. Considering the uncertainties itemized above, the percent uncertainty with the CB beam mode frequencies are [ ] percent to [ ] percent to obtain the following range of frequency:

- [ ]

### Uncertainty of the Level of Response of the CB at the LSP Elevation

From Table 4-9, the best estimate value for the displacement of the LSP for the full scale design during HFT is [ ] mil, rms. Considering the uncertainties itemized above, the percent uncertainty for the turbulent response of the CB beam mode is [ ] percent to [ ] percent to obtain the following interval of displacement:

- [ ]

This value is consistent with the results from the HYDRAVIB mockup testing with an offset of [ ] percent on the rms levels between the numerical and experimental results.

### Uncertainty of the Frequency of the HR Beam Mode

From Table 4-5, the best estimate value for the fundamental frequency of the HR beam mode (modes 3 and 4 or the "rocking modes") is [ ] Hz. Considering the uncertainties itemized above, the percent uncertainty with the HR beam mode frequency is [ ] percent to obtain the following range of frequency:

- [ ]

### Uncertainty on the Level of Response of the HR at Location / Elevation "HR\_A1"

From Table 4-9, the best estimate value for the displacement of the HR at the elevation or location "HR\_A1" for the full scale design during HFT is [ ] mil, rms. Considering the uncertainties itemized above, the percent uncertainty for the turbulent response of the HR beam mode is [ ]. Even in that extreme case, the contribution from the HR rocking motion is of

secondary importance and the uncertainties are almost unchanged compared to those for the LSP. So the [ ] percent interval of uncertainty obtained for the response of the CB at the LSP elevation is used here to obtain the following interval of displacement for the HR:

- [ ]

#### **Uncertainty on the Stress Levels in the CB**

The uncertainty in the computations for stress in the CB are directly proportional to uncertainties reported above for its dynamic response. Additionally, a FSRF of 3.0 is considered in the stress results reported in Section 4.2.7.1.2 to account for the peak stress effects created by the structural discontinuity of the CB cylinder and the CB flange. From Section 4.2.7.1.2, a peak stress of 850 psi, rms is reported. Considering the range of uncertainties reported above for the response of the CB, the following range of stress at the CB flange elevation is obtained:

- [ ]

This maximum stress is just less than four times the endurance limit of 4000 psi, rms at  $10^{10}$  cycles reported in Section 4.2.7.1.2. Therefore, high cycle fatigue failure is not predicted to occur.

#### **4.2.7.2 RCS Transient Conditions**

The turbulent responses of the RV lower internals to different combinations of RCP operation (i.e., one, two, or three RCP combinations) and the 10 percent RCP over-speed transient conditions that may occur during full power normal during operating conditions are not explicitly evaluated. Full scale analytical evaluations for FIV are not warranted for these short term transients where high cycle fatigue is the primary concern. However, based on the pre-operational vibration assessment for full power normal operating conditions, there is sufficient margin in the response of the RV lower internals to assert that the 10 percent RCP over-speed transient conditions are acceptable.

Applying the relationship for the dynamic pressure term, a 10 percent RCP over-speed transient condition will produce a 10 percent increase in the primary flow in the RV downcomer, which corresponds to a 21 percent increase in the response of the lower internals, or a scaling factor of  $1.21 (1.10)^2$ . Applying this scaling factor to the results reported in Section 4.2.7.1.1 and Section 4.2.7.1.2 for full power normal operating conditions and comparing the results to the allowable FIV limits justifies the 10 percent RCP transient.

The response of the RV lower internal assembly during the transients associated with the different combinations of RCP operation are measured during HFT to confirm acceptable vibratory behavior based on the acceptance criteria established in Section 4.2.6. The various tests that define HFT program are listed in Table 5-4 and include a variety of RCP transients that are performed at different operating temperatures. The RCP transients are normally

experienced during plant heatup and have a short duration and subsequently, the high cycle fatigue of the RV lower internals resulting from the turbulence in the downcomer is negligible.

However, the response of the full scale prototype design to the flow conditions in the RPV downcomer created by various combinations of RCPs operation and the non-symmetric loading to the RPV internals can be extrapolated from the experimental results from the HYDRAVIB mockup flow tests. Flow testing is performed with the HYDRAVIB mockup using different combinations and configurations of pump operation, the results of which are summarized in Table 4-37. This table reports the amplitudes of vibration that are measured with the displacement sensors located on the LSP for the 1<sup>st</sup> beam mode ([ ] Hz) of the CB and the broadband response for a frequency range from 0 Hz to 300 Hz.

With the exception of test 3, which is performed at elevated flow conditions, the largest response of the CB beam mode is for the four pumps configuration (test 2) where the narrow band response of [ ] mils, rms (40 – 75 Hz) is obtained. The largest broadband response (0 - 300 Hz) is for the two pump configuration (Tests 5, 6, 7, 8 and 9), with the maximum response measured for test 6. A comparison of the vibration amplitudes measured with test 2 (four pump) and test 6 (two pump) show that the broadband response increases from [ ] mil, rms to [ ] mils, rms, respectively.

Extrapolating the test results for the most limiting two pump operating configuration (test 6) determined with the 1 / 8.168 scale HYDRAVIB mockup to the full scale prototype design provides an LSP response of [ ] mils, rms, based on the broadband response. Based upon the results from the numerical model for HFT #17 provided in Table 4-9, Figure 4-23 and Figure 4-24, the acceptance criteria for stress and displacements are satisfied for this RCP transient condition. The relatively short duration of these RCP transients does not create significant high cycle fatigue concerns or excessive amplitudes of vibrations.

The response of the RV lower internal assembly to the RCP transients are measured during HFT to verify that these components do not experience significant amplitudes of vibration and stress to confirm that the high cycle fatigue resulting from these transients is insignificant. Further, the RV lower internal assembly are observed for the existence of abnormal vibrations during these RCP transients while adhering to the acceptance criteria established in Section 4.2.6, Section 5.5, and Section 6.1. Therefore, the development of an analytical response of the RV internal assembly to the flow excitations resulting from these transient conditions is not required to demonstrate the integrity of the RV internals to the high cycle fatigue concerns associated with these RCP transient conditions.

#### 4.2.8 Conclusions

The response of the lower internals to random turbulence is validated against mockup tests and a 1/8 scale numerical model. The 1/8 scale FEM model is then used to extrapolate results from

the mockup scale and cold conditions to the full scale reactor for hot functional tests and operating conditions. The model is also used to verify that no significant departure is expected between the empty and the full core configurations. The verification process for the full scale RV lower internals model conforms to the guidance of Reference 1.

The response of the RV lower internal assembly is [

] The static and the amplified response components of the [

]

The overall displacements remain within the range of past experience of the French N4 and German Konvoi RV designs of about [ ] mils, rms (or [ ] microns, rms) measured at the LSP and [ ] mils, rms (or [ ] microns, rms) measured at the HR upper lip (broadband), with statistical frequencies of about [ ] Hz.

#### 4.3 Flow Distribution Device (FDD)

The assessment for the vibratory behavior of the FDD is based on 1/8 scale flow testing and full scale theoretical analysis. The primary objectives of the testing on the FDD are as follows:

- To verify that an adequate distribution of the flow is created through the fuel bundle for various RCP operating combinations.
- To verify that vortices are not created by the FDD to avoid flow excitation from vortex shedding.
- To assess the hydrodynamic mass effects of the FDD by determining the in-air and the in-water experimental natural frequencies.

##### 4.3.1 Testing Performed for the FDD

Flow testing for the FDD is performed as part of the HYDRAVIB test program. The 1/8 scale FDD mockup is used to identify the horizontal, vertical and torsional modes for both the in-air and in-water environments at ambient temperature. The FDD is instrumented with accelerometers, as shown in Figure 4-47, and excited in different directions to determine the modal frequencies and mode shapes of the FDD. The modal frequencies for the 1/8 scale mockup of the FDD are reported in Table 4-11.

##### 4.3.2 Theoretical Analysis of the Flow Distribution Device

A full scale theoretical evaluation of the FDD is performed. The flow-induced vibration phenomenon of concern for the FDD is random turbulence excitation resulting from the downcomer flow going through and past the FDD. The narrow band acoustic pressure fluctuations associated with the RCP rotational speed ( [ ] Hz) and the pump blade passing frequency ( [ ] Hz) are also a potential source of excitation.

The measures identified in Section 4.2.5.2.2 for the lower internals are also implemented for the FDD to assess the excitation of the FDD to other sources of acoustic pressure fluctuations (e.g., acoustic resonance and loop acoustics).

The base excitation of the FDD resulting from the CB beam mode ( $\sim [ \quad ]$  Hz, See Table 4-5 and Table 4-6) is well separated from the beam mode of the FDD ( $\sim [ \quad ]$  Hz, See Table 4-12).  $[ \quad ]$  and is not represented in the theoretical analysis.

#### 4.3.2.1 Analysis Methodology and FIV Inputs

##### 4.3.2.1.1 Random Turbulence Induced Vibrations

The response of the FDD to turbulence is calculated assuming excitation of the cylindrical shell as well as the square grid plates. The response of the FDD to random turbulence due to parallel flow excitation of the thermal hydraulic conditions in the RV is calculated using the AREVA NP PC-based computer program "PCRANDOM." This program finds the response of a FEM to pressure PSDs based on finite element implementation of the acceptance integral method of Reference 7 and Reference 8.

The analytical method implemented to estimate the RMS response of the FDD follows the guidelines established in the ASME Appendix N-1300 (Reference 9a) and the equation shown below for parallel flow excitation of two dimension structures which, is taken from Reference 4, Equation 8.50.

$$\langle y^2(\vec{x}) \rangle = \sum_{\alpha} \frac{AG_p(f_{\alpha}) \Psi_{\alpha}^2(\vec{x}) J_{\alpha\alpha}(f_{\alpha})}{64\pi^3 m_{\alpha}^2 f_{\alpha}^3 \zeta_{\alpha}}$$

Where:

$\langle y^2(\vec{x}) \rangle$  = the mean square vibratory amplitude.

A = the surface area of the element or structure.

$G_p(f_{\alpha})$  = the single-sided fluctuating pressure power spectral density (PSD) in (force/area)<sup>2</sup>/Hz, due to turbulence.

$\Psi_{\alpha}^2(\vec{x})$  = the mode shape function of the structure.

$\alpha$  = modal index, two directions.

$J_{\alpha\alpha}$  = the joint acceptance integral of the structure.

$m_{\alpha}$  = the generalized mass.

$f_{\alpha}$  = the modal frequency in Hz.

$\zeta_{\alpha}$  = the modal damping ratio.

- | The PC program PCRANDOM determines the response PSD and then integrates this PSD with respect to the frequency to obtain the RMS response at the selected FEM nodal locations. The coding implemented by PCRANDOM to obtain the general response PSD is:

$$[ \quad ]$$

This equation may be rearranged to only calculate the desired diagonal PSD terms because the off-diagonal or response cross spectral densities are almost never needed. However, the revised equation neglects the possibility that a structure vibrating in one mode will change to another mode when excited by a random force. Cross modal participation can not occur if the natural frequencies of the component are well separated, as is the case for the FDD as shown in Table 4-12. This simplification does not have an impact upon the results obtained for the FDD. The following grouping of the response PSD equations uses the matrix "element-by-element" multiplication operation ( $\otimes$ ).

$$[ \quad ]$$

Where:

$$[ \quad ]$$

The following inputs are used by PCRANDOM to calculate the response PSD for the structure subjected to random turbulence using the coherence integral approach:

#### The in-water natural frequencies and mode shapes of the FDD structure

The in-water frequencies and mode shapes are determined with the AREVA NP "CASS" finite element program. The presence of the primary fluid surrounding the FDD induces a fluid-structure coupling which is taken into account by means of a hydrodynamic added mass. This added mass is determined from in-water testing of the FDD beam mode and is overestimated for the cylindrical shell modes of the FDD. However, this mass is conservatively considered with the shell modes of the FDD to provide a set of natural frequencies that are lower than expected and thus will experience a larger response to turbulent excitation. The cylindrical shell and the square flow channels of the FDD are modeled with plate elements. The support columns of the FDD were modeled with three dimensional beam elements. The in-water natural frequencies selected for FIV analysis are provided in Table 4-12.

#### The structural damping of the FDD structure

The structural damping ratio ( [ ] ) is set to two times the viscous damping ratio ( [ ] ) to achieve the equivalent structural damping at resonance. This total damping value is a conservative composite of the following damping mechanisms:

- Damping due to the non-linearity of the bolted connection between the FDD column supports and the lower core support plate.
- Damping due to the viscosity of the fluid.
- Damping associated with hysteresis, which is typically about 0.5 percent for stainless steel materials.

#### The pressure PSD function for parallel flow random turbulence excitation

The unique PSD for the turbulence in the RV lower plenum described in Section 4.2.2.4.3 is used for the FIV analysis of the FDD. The non-dimensional PSD is conservatively converted to a dimensional pressure PSD " $G_p(f)$ " considering the primary flow velocity and hydraulic diameter of the RV downcomer. The pressure PSD that is applied in the FIV analysis of the FDD is shown in Figure 4-29.

#### The convective velocity and the correlation length of the forcing function

The correlation lengths and convective velocities are used to calculate the matrix of coherence integrals based upon the definition for each pair of nodes in the FE model. The convective velocity is conservatively assumed to be [ ] of the nominal flow velocity ( [ ] ft/sec) through the FDD to create the greatest coincidence of phase relationship with the forcing functions and the modal frequencies of the FDD. The correlation length is

[ ] inches)  
and does not have any frequency or spatial dependency.

#### 4.3.2.1.2 Vibrations Induced by RCP Acoustic Pressure Fluctuations

The response of the FDD to the RCP acoustic pressure fluctuations is determined by traditional techniques of forced vibrations using the PC-based computer program EBDynamics. The PC-based program EBDynamics finds the time domain solution of coupled structure and fluid finite element models. The program also has the capability to find the solution for a structure-only model or a fluid-only model.

The EBDynamics model of the FDD reads the modal frequencies, stiffness and mass matrices of the finite element model of the FDD that are created with the execution of CASS in

Section 4.3.2.1.1. An assumed acoustic pressure fluctuation of [ ] (0-peak) is evaluated at the RCP rotational speed ( [ ] Hz) and the pump blade passing frequency ( [ ] Hz). The modal frequencies of the FDD (See Table 4-12 and Figure 4-27) that are most susceptible to the excitation of the RCP pressure fluctuations are;

$$f_{\text{beam}} = [ ] \text{ Hz (modes 1 and 2) and}$$

$$f_{\text{plate}} = [ ] \text{ Hz (mode 6)}$$

These modal frequencies are close to the RCP shaft and blade passing frequencies and the mode shapes are capable of being excited by acoustic pressure loading. The harmonic force that is representative of the RCP acoustic pressure fluctuations is applied to the EBDynamic model of the FDD.

To address the bias and uncertainties associated with the modal frequencies of the FDD, additional analyses are performed to determine the resonant response of FDD to the acoustic pressure fluctuations generated by the RCP blade passing frequencies. This resonant condition is most probable during the 10% RCP overspeed transient condition when the RCP blade passing frequency could increase to [ ] Hz ( $1.1 * [ ]$  Hz), which is in close proximity to the [ ] Hz plate mode of the FDD. If the actual frequency of the FDD plate mode varies due to differences in the material properties and the as-built dimensions, the two frequencies may be closer than the degree of separation that is identified, and potentially a resonant condition could exist.

**Table 4-11—Modal Frequencies of the 1/8 Scale FDD**



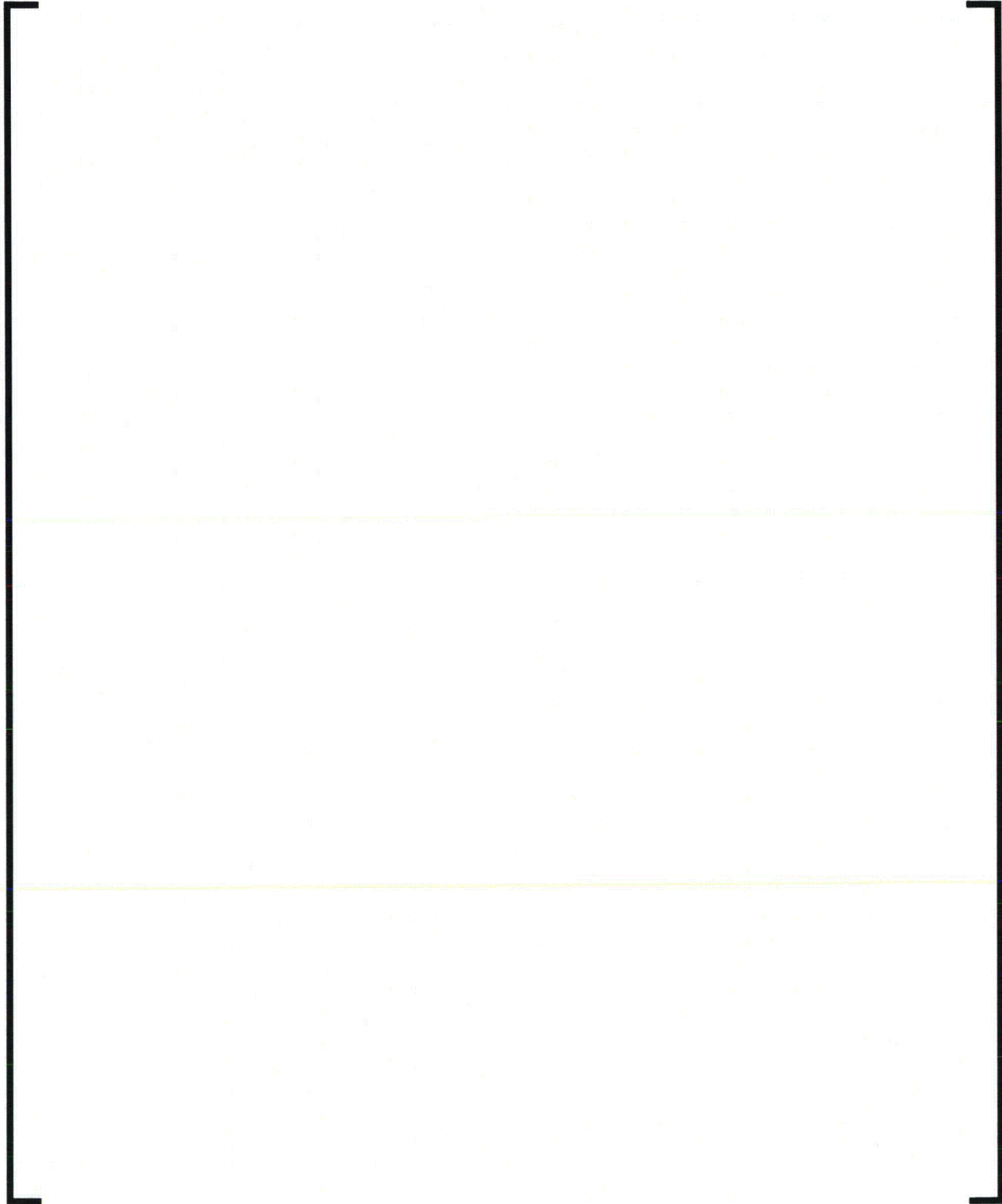
**Table 4-12—Modal Frequencies of the Full Scale FDD (In-Water)**

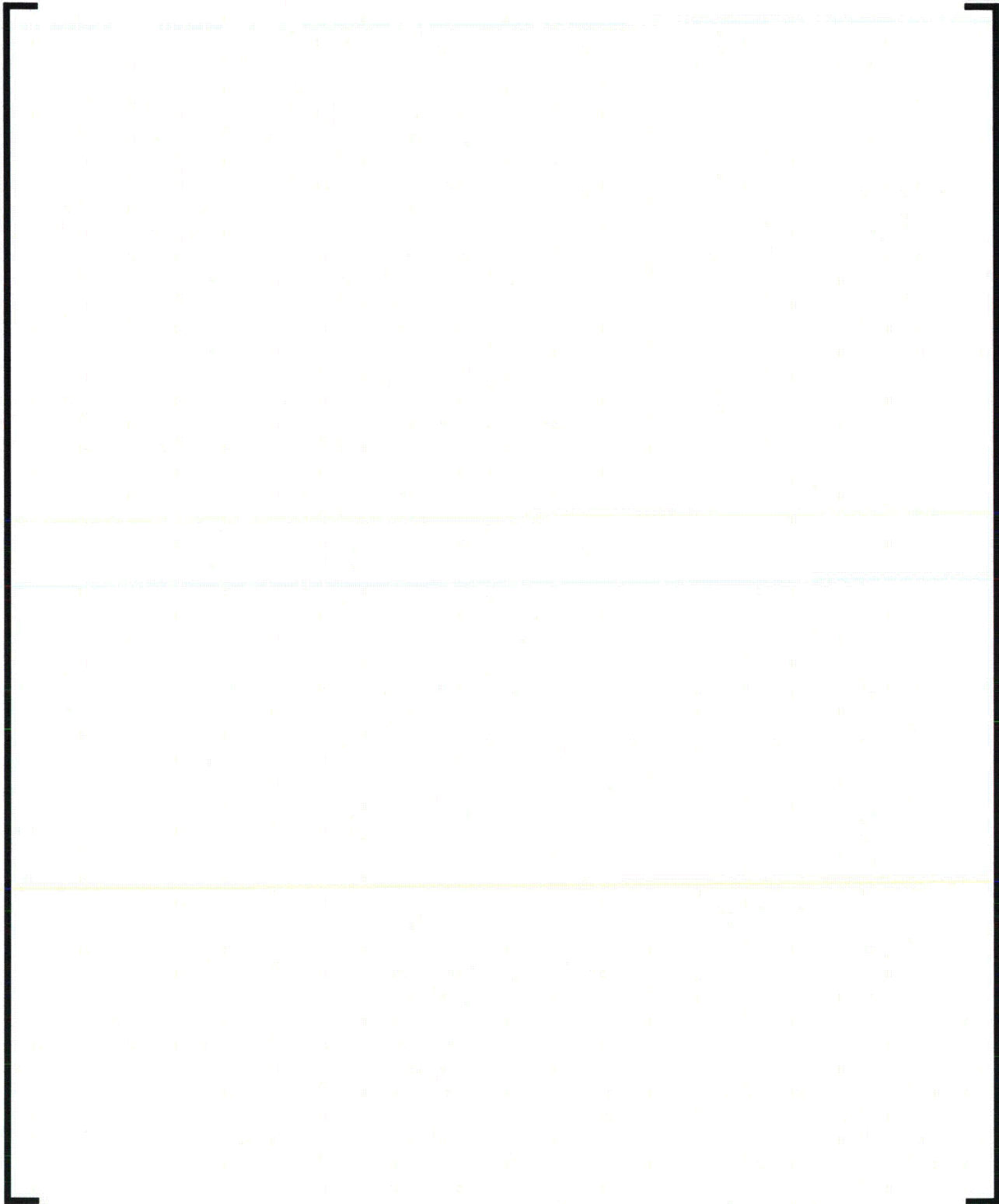


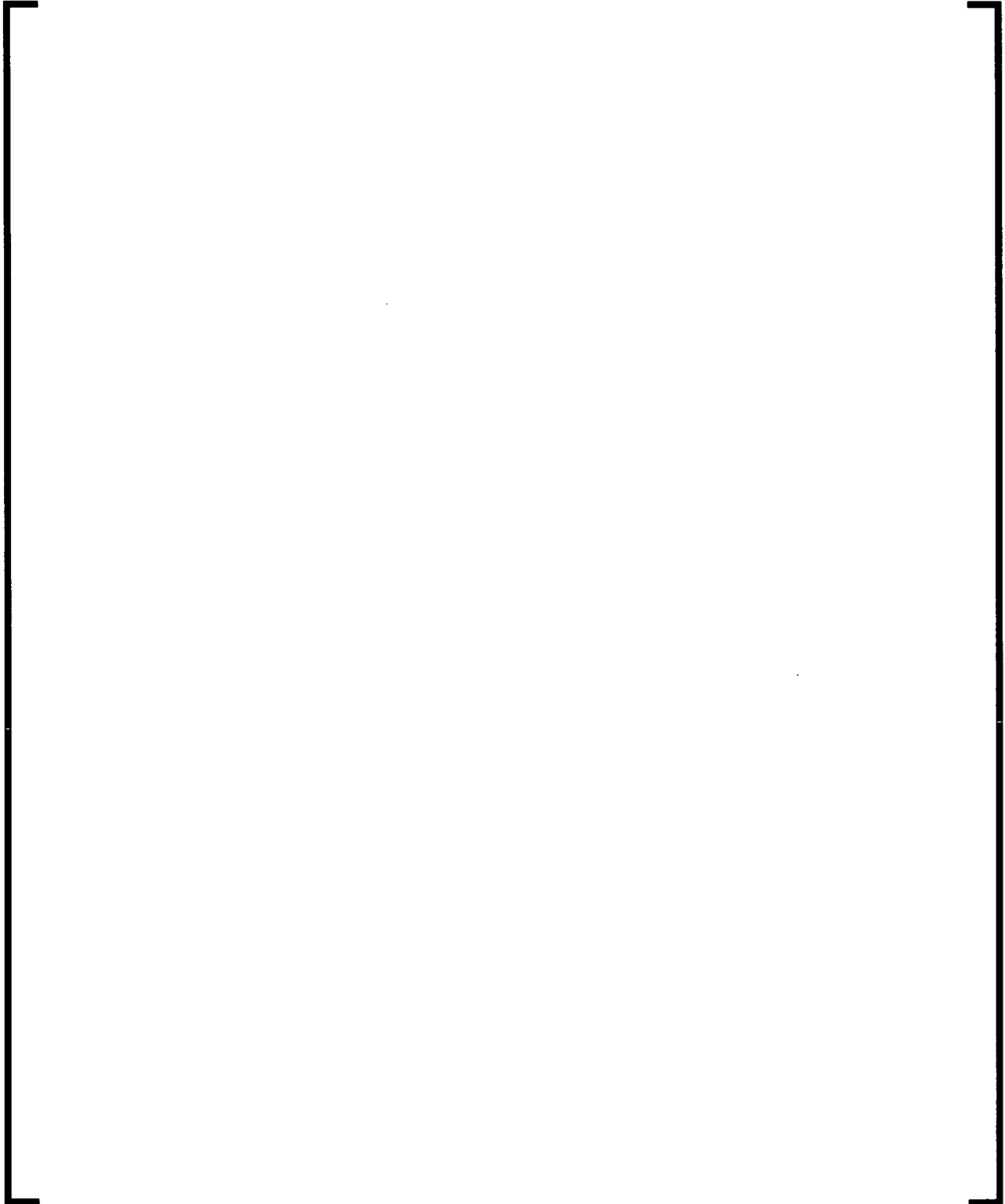
Notes for Table 4-12:

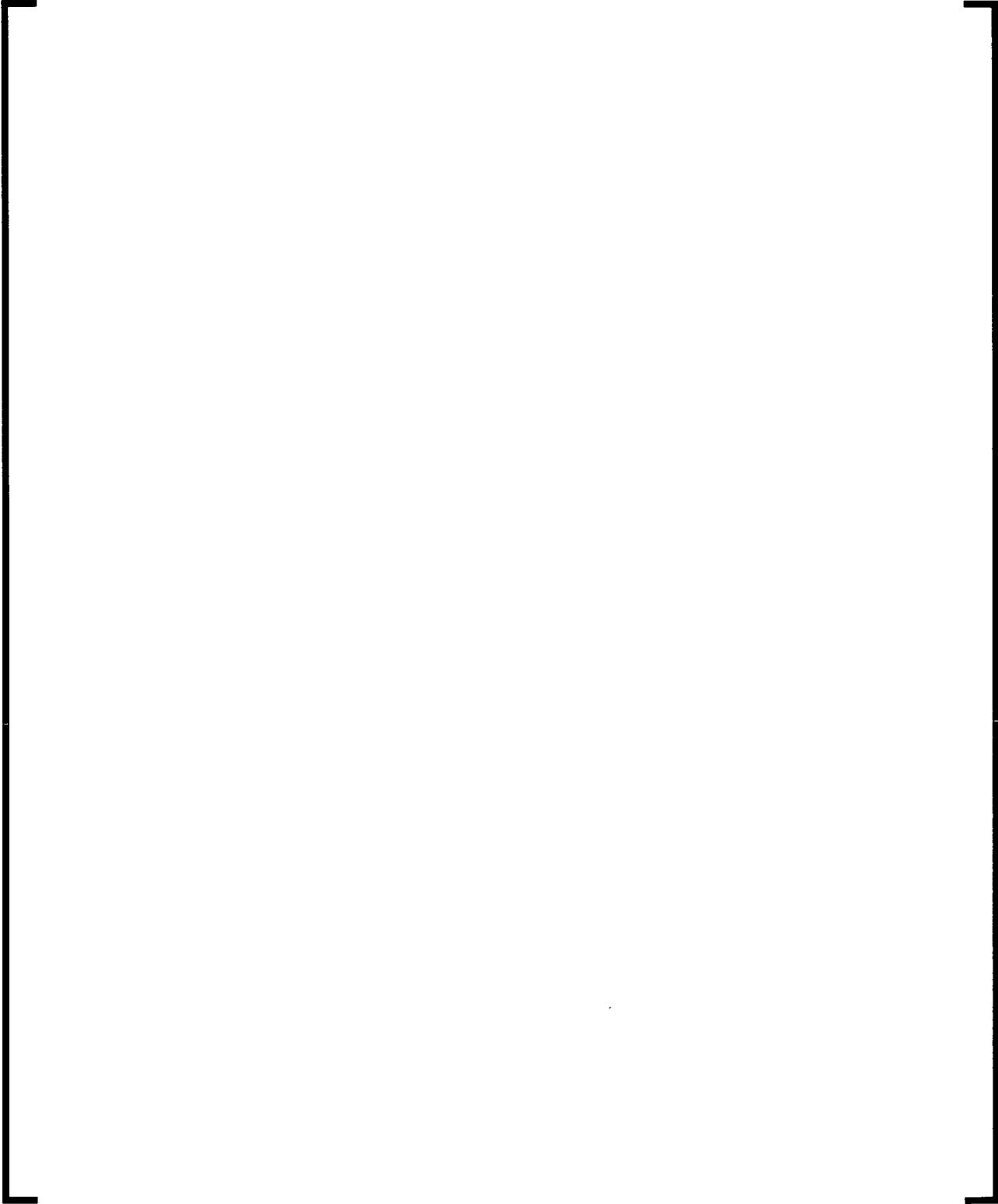
1. The mode shape plots for the ten modes for the full scale FDD are shown in Figure 4-27.

**Figure 4-27—Frequencies and Mode Shape Plots for the FDD**









---

**Figure 4-28—Deleted**

**Figure 4-29—Pressure PSD Loading for FDD (Log vs. Linear Scale)**



### 4.3.3 FIV Acceptance Criteria for FDD

#### 4.3.3.1 Acceptance Criteria for Displacements

Displacement limits are typically imposed to prevent impacts with the adjacent structures. Because such interfacing structures do not exist for the FDD, displacement limits for the FDD are not applicable.

#### 4.3.3.2 Acceptance Criteria for High Cycle Fatigue

The FDD is primarily fabricated from stainless steel type F304LN. The acceptance criterion for the stress and high cycle fatigue limits of the FDD for loading generated from random turbulence follows the rationale and methodology that is established for the RV lower internals in Section 4.2.6.2.

The primary plus secondary stress range ( $P_L + P_b + Q$ ) for the Level A & B service limits have not been determined. When these stresses are computed, the primary plus secondary stress range in the FDD, for which the alternating FIV stress is cyclic, will be less than 27.2 ksi. Therefore, fatigue curve "A" of the ASME code is justified for the FDD since there are no welds located within three wall thickness of the stress location (i.e., the FDD is a forged component). The allowable stress for fatigue curve "A" is [ ] psi, rms at  $10^{13}$  cycles. (See Figure 4-21).

Since, the response of the FDD to the RCP acoustic pressure fluctuations is determined in units of psi (0-peak), the allowable high cycle fatigue stress is [ ] psi (0-peak) at  $10^{11}$  cycles which is based upon fatigue curve "A".

#### 4.3.4 Response of the FDD

The response of the FDD to the turbulence in the RV lower plenum resulting from the full power, steady normal operating condition and the acoustic pressure fluctuations associated with the RCP blade passing frequencies is reported in this section. The response of the FDD during HFT (Test #17, See Table 5-4) is assessed based upon the results for the full power normal operating condition and the ratio of the dynamic pressure term between the two operating conditions or ( [ ] ).

The results show that the FIV acceptance criteria established in Section 4.3.3 for the FDD are satisfied.

##### 4.3.4.1 Response of FDD to Random Turbulence

The displacement response PSD of the FDD at seven nodal locations around the circumference of the cylinder is shown in Figure 4-30. The figure shows the response at each of the natural frequencies of the FDD with a major response occurring at the fundamental frequency ( [ ] ).

]). A significant response of the shell mode ( [ ] ) is also shown.

The RMS responses at the seven node locations are listed in Table 4-13. The table shows that the responses at [ ]

At the other two locations

( [ ]

]

The statistical frequencies for the FDD are zero crossing frequencies. The zero crossing frequency is defined as the number of times per second the response curve crosses the zero response line (assuming the mean has been subtracted out). This effective frequency is determined using the relationship shown below considering the weighted integrals of the single-sided displacement response PSD,  $G_d(f)$ :

$$f_0^2 = \frac{\int_0^{\infty} f^2 G_d(f) df}{\int_0^{\infty} G_d(f) df} \quad \text{definition of the zero crossing frequency.}$$

The AREVA NP computer program "PCRANDOM" uses this definition to determine the zero crossing frequencies. The crossing frequencies reported in Table 4-13 for the discrete locations along the circumference of the FDD cylindrical shell are below the fundamental frequency of the FDD. The reason for this discrepancy is based on the method by which the effective zero crossing frequencies are computed by PCRANDOM through the weighting of the integral of the single-sided displacement response PSD,  $G_d(f)$ . Because the effective zero crossing frequency is determined by the integration of the response PDS between 0 and approximately 225 Hz, the weighting of the PSD at the lower frequencies (below the fundamental frequency of the FDD) skews this computation.

#### 4.3.4.1.1 FDD Support Column Stress

The support column moments at the fixed locations are reported for six of the 24 support columns in Table 4-14. Because the FDD is a symmetrical structure, the moments from the six columns (one quadrant) define the behavior of the FDD. The highest bending stress in the support column is [ ] psi, rms. Assuming a conservative value of [ ] for the FSRF to account for discontinuities, the maximum rms stress is [ ] psi, rms.

Considering the beam modal frequency of the FDD ( [ ] Hz, See Table 4-12), a 60 year life and a capacity factor of 100 percent, an endurance limit of [ ] rms is obtained from Figure 4-21. A safety factor of [ ] for the FDD support columns, and high cycle fatigue failure of this component is not expected.

#### 4.3.4.1.2 Support Column Reaction Forces

The reaction forces and moments are reported at the fixed nodal locations for six of the 24 support columns as shown in Table 4-15. These are the same node locations at which the support column stresses are reported in Table 4-14. The results show that the reaction forces at the support column attachment locations [ ]

#### 4.3.4.1.3 FDD Cylindrical Shell Stresses

The principal stresses at the centroid of the cylindrical shell plate elements are obtained to evaluate the potential for fatigue damage to the FDD. For each of the plate elements shown in Figure 4-32, the two principal stresses (S1 and S2) are calculated at the centroid of each element. These alternating stresses are calculated at both the inside and outside surfaces. Table 4-16 shows the principal stresses and demonstrates [ ] is not expected.

#### 4.3.4.2 Response of the FDD to the RCP Acoustic Pressure Fluctuations

The response of the FDD to the RCP acoustic pressure fluctuations for the off-resonant ( [ ] Hz) and resonant ( [ ] Hz) conditions is provided in this section. The resonant response of the FDD plate mode ( [ ] Hz) to the acoustic pressure fluctuations generated at the same blade passing frequency is provided to evaluate the bias and uncertainties associated with the modal frequencies and the response of the FDD to this source of excitation. The summary of results provided in Table 4-16A compares the off-resonant and resonant response of the FDD that is created from the two forcing functions;

$$\Delta P = [ ] \text{ psi (0-peak) at } [ ] \text{ Hz}$$

$$\Delta P = [ ] \text{ psi (0-peak) at } [ ] \text{ Hz}$$

The stress results provided in Table 4-16A are for the most limiting locations and do not include the stress amplification effects of the structural discontinuities of the FDD. Assuming a conservative value of 4.0 for the FSRF, a maximum alternating stress of [ ] psi (0-peak) is obtained for the resonant loading condition ( $\Delta P = [ ]$  psi at [ ] Hz). Since this stress amplitude is much less than the endurance limit of [ ] psi (0-peak) at  $10^{11}$  cycles for SS 304-LN, high cycle fatigue failure is not expected for the FDD structure.



**Table 4-14—Maximum Stress in the FDD Support Columns Due to the Response of the FDD to Random Turbulence**

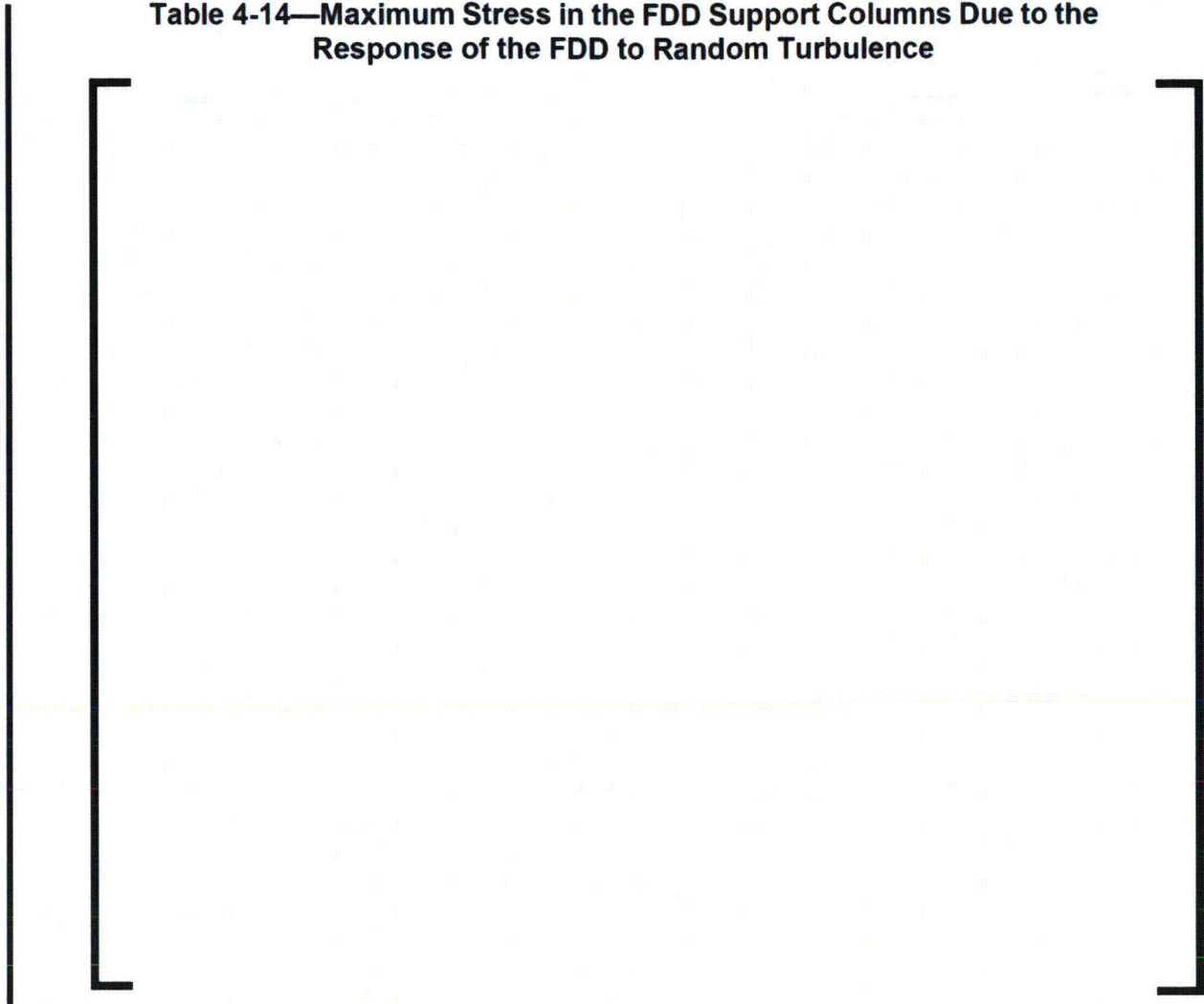


**Table 4-15— Reaction Loads in the FDD Support Columns Due to the Response of the FDD to Random Turbulence**

A large empty rectangular area enclosed by thick black brackets, indicating that the table content is missing or redacted.

**Table 4-16—FDD Stress in the Cylindrical Shell Due to the Response  
of the FDD to Random Turbulence (psi, rms)**

A large rectangular area is enclosed by brackets on the left and right sides, indicating the location of a table. The table itself is empty.

Notes for Table 4-16:

1. See Figure 4-32 for element locations.

---

**Table 4-16A—Response of the FDD to the RCP Acoustic Pressure Fluctuations**

--

**Figure 4-30—FDD Cylindrical Shell Response PSD**



**Figure 4-31—Nodal Locations for the Shell Response PSDs**

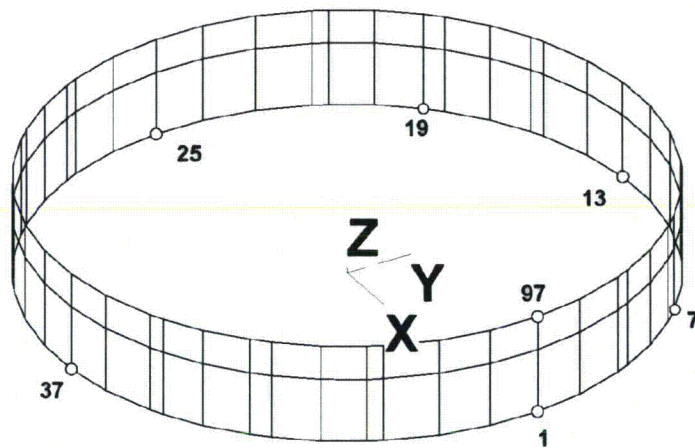
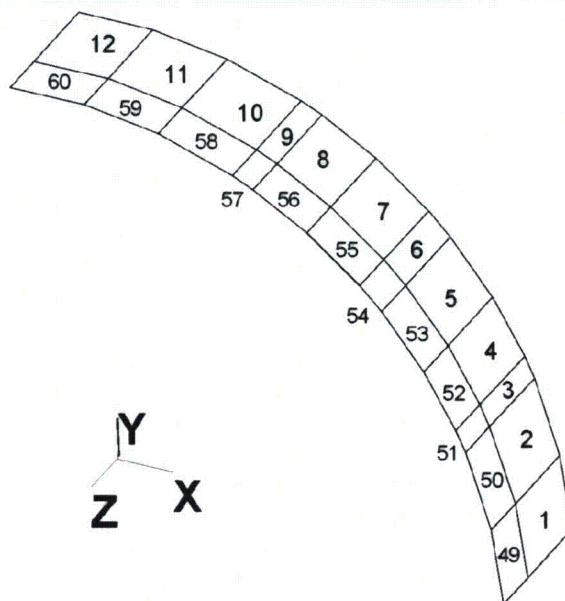


**Figure 4-32—FDD Cylindrical Shell Elements for Evaluation of Stress**



#### 4.3.5 Conclusions

The results from the analysis for turbulence show that the FIV performance of the FDD is acceptable for the full power, steady state normal operating conditions. The stresses in the cylindrical shell and square flow channels are significantly below the allowable stress. Additionally, the reaction loads at the supports of the FDD that result from the FIV response of the FDD are minimal. It is not possible for the bolted connections between the FDD and the LCP or at the tie rod connections between the LCP and the HR to separate and create additional cyclic loading on these members.

The results from the analysis of the FDD for the forced vibrations created by a RCP acoustic pressure fluctuation show that both the off-resonant and the resonant response of the FDD are insignificant during full power, steady state normal operating conditions. The response of the FDD to the resonant conditions between the RCP blade passing frequency and the FDD frequency (mode 6, [ ] Hz) demonstrates that any bias or uncertainty that may exist in the modal frequencies or the response predicted for the FDD for this source of excitation does not create unacceptable vibrations.

Based on the large margin of safety for the FDD at the full power normal operating conditions, there is ample margin for this component during the following RV transient conditions:

- 10 percent RCP overspeed transient conditions that may occur during full power normal operating conditions.
- Different combinations of RCPs operation (i.e., one, two, or three RCP combinations).

Explicit analytical evaluations of the short term transients are not performed. These transient conditions are evaluated as follows:

Because a 10 percent RCP overspeed transient condition produces a 10 percent increase in the primary flow through the FDD, this corresponds to a 21 percent increase in the response of the FDD or a scaling factor of 1.21  $(1.10)^2$  based on the relationship for the dynamic pressure term. Applying this scaling factor to the results reported in Section 4.3.4 for full power normal operating conditions and the allowable FIV limits provides justification for this RCP transient.

As summarized in Section 4.3, [

] The response of the FDD to transient conditions associated with the different combinations of RCP operation are measured during HFT to confirm acceptable vibratory behavior based on the acceptance criteria established in Section 4.3.3, Section 5.5, and Section 6.1. Additionally, as described in Section 4.2.7.2 for the RV lower internal assembly, the measurements and inspections performed as a part of HFT confirm acceptable behavior of the FDD to these RCP transients.

#### 4.4 Irradiation Specimen Basket

The design of the irradiation specimen basket that is installed in the RV downcomer of the U.S. EPR has a substantial degree of operational experience that would allow its classification as a non-prototype design. The flow testing and analytical rigors outlined in Reference 1 are not applicable to the irradiation specimen basket. However, the design of the basket is reviewed for susceptibility to potential FIV mechanisms.

##### Random Turbulence Excitation

The natural frequencies of the three major components of the specimen basket assembly (the guide support, the guide base, and the guide cap) are calculated. The calculations show that the lowest natural frequency for the assembly is [ ] Hz for the guide base. Because the turbulent excitation and the associated coherence at such a high frequency is extremely small, the turbulence excitation resulting from cross flow conditions is not a concern. Therefore, detailed flow-induced vibration evaluations are not performed. Further, turbulent excitation resulting from parallel flow conditions, which is typically an order of magnitude less in comparison to excitation from cross flow conditions, is not applicable for this component.

##### Vortex-Shedding Excitation

Based on the configuration of the specimen basket assembly and its orientation in the RV downcomer, alternate shedding of vortices past the assembly is not possible. The irradiation specimen basket is vertically oriented in the RV/CB annulus (See Figure 2-1). The flow conditions in this region of the downcomer have both axial and circumferential orientations so that if vortices were capable of forming downstream of the irradiation basket assembly, they would be disrupted by the other component of flow in RV annulus and prevent the organization of the vortices and lock-in conditions with the structural frequencies of the basket assembly.

##### Acoustic Pressure Fluctuations

The low frequency pressure fluctuations associated with loop oscillations or loop acoustics do not have the capability to excite the specimen basket assembly. These pressure fluctuations are typically associated with the momentum changes of the primary fluid as it enters the RV downcomer and exhibit a relatively large magnitude and are completely coherent. Excitation of the large structures (i.e., the CB) is possible under the appropriate circumstances. Because there is a large separation of frequencies between the specimen basket and these acoustic pressure fluctuations, the off resonant excitation of the specimen basket are insignificant.

Additionally, the wave length of these acoustic pressure fluctuations ( [ ] ) is significantly larger than the dimensional length of the specimen basket. Therefore, it is not possible for this relatively short structure to experience significant excitation from this acoustic pressure fluctuation.

The acoustic pressure fluctuations associated with the RCP blade passing frequencies, approximately [ ] psi (0-peak) at the blade passing frequency of [ ] do not have the potential to excite the specimen basket. The lowest natural frequency of the specimen basket is [ ] Hz, which is well separated from the blade passing frequencies. This acoustic pressure fluctuation is also 100 percent coherent, but with a smaller magnitude than the loop acoustic discussed above. Therefore, the off-resonant excitation of the specimen basket to the RCP pressure fluctuations is insignificant and a detailed analytical evaluation is not required for either of these acoustic loadings.

#### Axial Leakage Flow Excitation

In the presence of a narrow flow channel surrounded by flexible structures, axial leakage flow-induced vibrations or instability could become a source of excitation. The guide cap has an open flow channel that allows primary flow to pass by the material specimen. The guide cap channels are plugged to capture the material specimens but do not inhibit flow through the guide cap. The radial clearance between the guide cap (ID) and the material specimen (OD) do not create a narrow flow channel. Additionally, the surrounding structures (i.e., guide cap and material specimen) are very stiff, and axial leakage instability does not occur with this design. This assertion is substantiated by the service life of this specimen basket design, which has been used in Europe and has not shown any evidence of FIV related problems.

### **4.5 RV Upper Internals**

The assessment for the vibratory behavior of the upper plenum internals is based upon (1 / 5.2) scale flow testing and full scale theoretical analysis. The primary objectives of the testing performed for the upper internals are:

- To provide an assessment of the maximum hydraulic load on the upper plenum columns of the RV internals.
- To qualify the computational fluid dynamic (CFD) model of the ROMEO mockup and the associated computations of the full scale design.

Given the simple design of the column supports in the RV upper internals and the degree of industry data available for these beam type members, it is not necessary to perform extensive testing to develop the FIV inputs that would allow the response of the upper columns support to be predicted within a reasonable degree of accuracy. A dynamic analysis of the scale model of the column supports is not performed. However, the (1/5.2) scale CFD model of the ROMEO mockup is benchmarked with the flow tests to aid in the development of the full scale CFD model of the RV upper internals which ultimately provides the thermal hydraulic inputs for the FIV evaluation.

#### **4.5.1 Theoretical Analysis of the RV Upper Internals (Full Scale)**

The full scale theoretical analyses of the upper plenum internals is performed for the following components:

- CRGA column supports.
- Normal column supports.
- Level measurements probe column supports.
- Instrumentation guide tubes.

The UCP and the USP are not susceptible to significant excitation from turbulence or any other FIV mechanisms. First, the rigidity offered by the column supports and the thickness of these plates increases the plate frequencies, making them less susceptible to turbulence. Second, the turbulence in the parallel flow through the UCP does not have the ability to become coherent with these high frequencies. Therefore, there is minimal potential to excite the modal frequencies of the UCP and USP.

The acoustic pressure fluctuations associated with loop acoustics do not have the ability to create significant excitation of the column supports (e.g., the CRGA columns, normal columns, LMP columns). The long wave length associated with the low frequency characteristics of loop acoustics makes the relatively slender structures of these upper internal components immune to this source of acoustic pressure fluctuations.

The narrow band acoustic pressure fluctuations generated by the RCP rotational speed ( [ ] Hz) and the pump blade passing frequency ( [ ] Hz) are typically less than 1 psi (0-peak). The long wave length associated with these pressure fluctuations make the relatively slender structures of these upper internal components immune to this source of acoustic pressure fluctuations. However, due to the close proximity of some of the harmonic frequencies of the RCP and the column supports, harmonic forced vibrations analysis of the column supports is performed. The column supports and the instrumentation guide tube are evaluated for a [ ] psi (0-peak) amplitude of pressure at the first shaft and blade passing frequency of the RCPs. The pressure fluctuations associated with the higher order harmonics are typically one order of magnitude less than the magnitude for the first shaft and blade passing frequency and therefore, a [ ] psi (0-peak) amplitude of pressure is evaluated for the second and third order harmonics of the shaft and blade passing frequencies.

The measures identified in Section 4.2.5.2.2 (and Appendix A.2.1) regarding the screening criteria to identify sources of acoustic resonances in the reactor coolant piping system verifies that the UCP, the USP, and the column supports are not excited by acoustic mechanisms.

The flow-induced vibration phenomena of concern for the column supports, which are cylindrical structures exposed to cross flows in the upper plenum include:

- Vortex-shedding induced vibration.
- Fluid-elastic instability.
- Random turbulence induced vibration.

The full scale theoretical analysis of these FIV mechanisms is performed considering a range of compressive axial loads to evaluate the sensitivity of the column supports to these sources of flow excitation.

The column supports are evaluated for the thermal hydraulic conditions representative of full power steady state operating conditions. The steady state flow conditions are augmented to effectively evaluate the 10 percent RCP overspeed transient condition by conservatively increasing the flow velocities by 10 percent (relative to the full power steady state normal operating condition) while still considering the high cycle fatigue associated with 60 EFPY with a 100 percent capacity factor.

The requirements of RG 1.20 (Reference 1) require that the transient conditions associated with RCP transients be evaluated. For these transients, flow reversal through one to three hot leg nozzles will occur, depending upon the combinations of RCPs that are being operated. The largest flow reversal, in terms of volume or flow velocity through the hot leg nozzle, occurs with three (3) RCP operating at the 75% power level. However, the largest dynamic pressure occurs with three (3) RCP operating at cold shutdown condition (370 psia, 140F). Since it is the dynamic pressure term that is the most appropriate parameter to compare, the RCP transient at cold shutdown is evaluated.

#### 4.5.1.1 Analysis Methodology and FIV Design Inputs

##### 4.5.1.1.1 Modal Analysis

The natural frequencies of the column supports are determined using the structural analysis program CASS with three dimensional beam elements. The frequencies and eigenvectors of the column supports are determined in the water environment at the full power operating temperatures. The effects of the hydrodynamic mass of the primary fluid on the in-air natural frequencies of the column support are accounted for by calculating an equivalent specific mass using the following formula:

$$[ \quad ]$$

For an infinite cylindrical tube, the displaced water corresponds to the water contained by the inner surface of the cylinder and the water displaced by the outer surface of the cylinder. The hydrodynamic mass per unit length of the displaced water is then:

$$[ \quad ]$$

#### 4.5.1.1.2 Vortex-Shedding Induced Vibrations

All three column types and the instrumentation guide tubes are evaluated for their susceptibility to experience vortex shedding induced vibration. The vortex shedding frequencies of these structures are determined from the relationship:

$$f_s = \frac{S_t V}{D}$$

Where:

V = the free stream flow velocity approaching the cylinder of a diameter "D."

$S_t$  = the dimensionless Strouhal number, which is dependant upon the Reynolds number.

The correlation between the Strouhal number and the Reynolds number is shown in Figure 4-33 for a single cylinder exposed to cross flow conditions (e.g., the instrumentation guide tube). For the other column types, the Strouhal number for the array of column supports is determined from the correlation shown below for a triangular array of cylinders, which is taken from Reference 4, Section 6.6:

$$S = \frac{1}{1.73(P/D - 1)}$$

Where:

P/D = the pitch to diameter ratio.

This expression for the Strouhal number is based on the approach velocity rather than the pitch velocity for which the thermal hydraulic data from the CFD model is provided. The Strouhal number expressed in terms of pitch velocity is:

$$S_p = \frac{1}{1.73(P/D)}$$

For cases of off resonances between the vortex shedding frequencies and the structural frequencies, the response of the column supports and the guide tube(s) to vortex-shedding excitation is determined through relationships for forced harmonic vibrations, considering the forcing functions in both the lift ( $F_L$ ) and drag ( $F_D$ ) directions given by:

$$F_L = (\rho V^2 / 2)(D)(C_L) \sin(2\pi f_L t) \quad \text{per unit length}$$

$$F_D = (\rho V^2 / 2)(D)(C_D) \sin(2\pi f_D t) \quad \text{per unit length}$$

The amplification factor, "A<sub>o</sub>" of these dynamic loads is equal to:

$$A_o(f) = \frac{1}{\{[1 - (f/f_o)^2]^2 + 4\zeta^2(f/f_o)^2\}^{1/2}}$$

For closely spaced arrays of cylinders with the pitch to diameter (P/D) spacing less than about 1.5, the distinct frequency associated with vortex-shedding degenerates into broadband turbulence. For the CRGA array of cylinders, the P/D ratio is equal to 1.26. The span wise variation of the velocity profile along the length of the support columns also reduces the strength of the lock-in.

Nonetheless, the support columns and the instrumentation guide tubes are evaluated for lock-in using the design methods outlined in Reference 9a to verify that a resonance condition between the natural frequencies of the column supports and the vortex shedding frequencies of the supports is avoided and that lock-in conditions do not occur. For a single cylinder (e.g., the instrumentation guide tube), lock-in can be avoided by any one of the four following methods. For an array of cylinders (the three column support type), only the first three bullets are applicable.

The design criteria used to verify that the lock-in condition is either avoided or suppressed for these structures are:

- a. If the reduced velocity for the fundamental vibration mode (n=1) satisfies the condition:

$$\frac{V}{f_n D} < 1, \text{ then both the lift and drag directions lock-in are avoided.}$$

- b. If the reduced damping (for a given vibration mode) is larger than 64:  $C_n > 64$ , then lock-in is suppressed for that vibration mode.

- c. For a given mode of vibration, the two following conditions are verified:

$$\left\{ \begin{array}{l} V/f_n D < 3.3 \\ C_n > 1.2 \end{array} \right\}$$

then the lift direction lock-in is avoided and drag direction lock-in is suppressed.

- d. For the structural frequencies, verify:  $f_n < 0.7f_s$  or  $f_n > 1.3f_s$ , where  $f_n$  is the natural structural frequency of the n<sup>th</sup> mode and  $f_s$  is the frequency of the periodic vortex shedding in either the lift or drag directions.

The reduced damping of the n<sup>th</sup> mode is equal to:

$$C_n = \frac{4\pi\xi_n M_n}{\rho D^2 \cdot \int_{L_c} \phi_n^2(x) dx}$$

Where:

$\xi_n$  = the damping of the  $n^{\text{th}}$  mode.

$\phi_n$  = the mode shape function of the  $n^{\text{th}}$  mode.

$L_e$  = the cylinder length subject to lock-in cross flow.

$M_n$  = the generalized mass of the  $n^{\text{th}}$  mode or  $M_n = \int_0^L m_t(x)\phi_n^2(x)dx$

$D$  = the cylinder diameter.

$\rho$  = the mass density of the primary fluid.

The damping inherent to the column supports is created by the viscous damping of the fluid (i.e., fluid damping due to fluid drag), the structural damping of the material (or hysteresis), and the damping associated with the non-linear interaction between the bolted connections of the columns with the UCP and USP. The damping for the column supports is determined from the following relationship, which is applicable to power plant piping. This correlation is a result of an extensive compilation of damping data of pipe sizes ranging from 1 to 18 inches. A regression analysis performed on the data provided the damping correlation shown below, which is taken from Reference 2, Equation 8-43.

$$\zeta = 0.0053 + 0.0024D + 0.0166R + 0.009F - 0.019L$$

Where:

$D$  = the diameter of the column support (in inches).

$R$  = the response level, equal to zero (0) if there is no yielding and one (1) if the amplitude is sufficient to cause yielding.

$F$  = 1 for the first mode ( $N = 1$ ) and 0 for the higher modes.

$L$  = 0 if the piping is relatively uniform and equal to 1 if relatively massive valves or other attached equipment is attached to the piping.

This damping relationship is used to determine the modal damping ratio for the normal, LMP and CRGA column supports as summarized in Table 4-17. An equivalent viscous damping ratio of [ ] percent that is associated with hysteresis is applied to the instrumentation guide tube since this component is welded to the supports.

#### 4.5.1.1.3 Fluid-elastic Instability

Reference 9a, paragraph N-1331.2 provides a criterion in which fluid elastic instability can be avoided for a tube bundle. This criterion is applied to the upper internals to predict fluid-elastic instability for the array of CRGA columns, normal and LMP column supports, and the instrumentation guide tube, and is based on the prediction of a critical velocity that must not be

exceeded. Connors' equation predicts that a tube or cylinder will become unstable if the mode-shape weighted secondary side pitch velocity that is defined by:

$$\bar{V}_{pn}^2 = \frac{\frac{1}{\rho_0} \int_0^L \rho(x) V_p^2(x) \psi_n^2(x) dx}{\frac{1}{m_0} \int_0^L m_t(x) \psi_n^2(x) dx}$$

exceeds a critical velocity of

$$V_c = \beta f_n \left( \frac{2\pi \zeta_n m_t}{\rho} \right)^{1/2}$$

Where:

$\rho_0$  and  $\rho(x)$  = the average fluid density and the density as a function of axial location along the length of the column.

$V_p$  = the pitch or gap velocity.

$\psi(x)$  = the mode shape function.

$m_0$  and  $m_t(x)$  = the average total linear mass and the total linear mass of the column support as a function of the axial location along the length of the column.

$\beta$  = the Connors' constant.

$f_n$  = the modal frequency, Hz.

$\zeta_n$  = the damping ratio on a modal basis.

A conservative Connors' constant of [ ] and a modal damping ratio of [ ] (viscous) are conservatively applied to the CRGA columns, [ ] Reference 9a, paragraph N-1331.3.

For flow reduced damping  $m(2\pi\zeta)/\rho D^2$ , which prevails in heavy fluids such as water, the instability mechanism is controlled by the fluid velocity mechanism (fluid-damping controlled). In this case, fluid coupling is not necessary to cause instability. The effect of detuning or the differences in the frequencies between the normal and LMP columns and the adjacent CRGA column supports do not have a significant effect upon the critical velocity of the CRGA columns.

The analysis for fluid-elastic instability is based on these correlations using the AREVA NP computer program PCSTAB2. To determine the margin of safety against fluid-elastic instability, AREVA NP has defined a parameter called fluid-elastic stability margin (FSM), which is the ratio of the critical velocity to the mode shaped weighted pitch velocity:

$$FSM = V_c / V_{pn}$$

If the FSM is less than 1.0, the array of column supports is predicted to be unstable, while an FSM that exceeds 1.0 indicates that the column supports will be stable. The value of FSM above 1.0 represents a margin of safety in the usual engineering sense. The acceptance criterion for fluid-elastic instability for the U.S. EPR is an FSM greater than 1.3. The fluid-elastic instability ratio ( $V_{pn} / V_c$ ) is simply the inverse of the AREVA NP definition for FSM.

#### 4.5.1.1.4 Random Turbulence Induced Vibrations

The analysis for random turbulence-induced random vibration, or turbulent buffeting, resulting from cross flow conditions is based on finite element implementation of the acceptance integral method of References 7 and 8 using the computer program PCRANDOM. The methodology implemented by PCRANDOM to determine the RMS response of the columns supports is described in Section 4.3.2.1.

The column supports are evaluated as a one dimensional beam based on the conservative assumption that the random pressure is fully coherent across the diameter of the columns. The empirical relationship for the turbulent response of a one dimensional structure, or in this case, the column supports, is defined below and is consistent with the guidelines established in Reference 9a, Paragraph N-1340.

$$\langle y_n^2 \rangle = \sum_n \frac{L G_F(f_n) \Phi_n^2(x)}{64\pi^3 m_n^2 f_n^3 \zeta_n} J_{mn} + \text{cross terms}$$

Where:

$\langle y_n^2 \rangle$  = the mean square vibratory amplitude.

L = the column length.

n = a modal subscript.

$G_F(f_n)$  = the single sided random force PSD.

$\Phi_n(x)$  = the mode shape function along the length of the column.

$m_n = \int_0^L \Phi_n^2(x) m(x) dx$  or the generalized mass.



is ~ [ ] inch, which is a relatively large value. The structural damping coefficient is set to two times the viscous damping coefficient ( [ ] ) to achieve the equivalent structural damping at resonance.

#### 4.5.1.1.5 RCP Acoustic Pressure Fluctuations

The largest amplitude and resulting acoustic pressure typically occurs with the first blade passing frequency and will vary between  $-\Delta P/2$  and  $+\Delta P/2$  in a distance equal to the wave length of the acoustic pressure fluctuation. The wave length ( $\lambda$ ) of the acoustic pressure fluctuations depends on its frequency and will vary for each RCP tone, but in general are very long wave lengths. Referring to Figure 4-59, the pressure differential ( $\Delta p$ ) that is imparted to these cylindrical structures with a diameter,  $d$ , by an acoustic pressure fluctuation with a magnitude equal to  $\pm p_o$  and a wave length,  $\lambda$ , is equal to;

$$\Delta p = \frac{2p_o d}{\lambda} \text{ psi}$$

and creates a harmonic force on the cylinder equal to;

$$F = d\Delta p = \left(\frac{2d}{\lambda}\right)p_o d \text{ per unit length}$$

The characteristics of the acoustic pressure fluctuations and the static loads that are created by the normal impingement of the RCP acoustic pressure fluctuations upon the column supports are provided in Table 4-30 and Table 4-31, respectively. The amplification factors reported in Table 4-33, determined with the methods and damping ratios provided in Section 4.5.1.1.2, are used to generate the harmonic excitation forces acting on the column supports.

Significant excitation of the support columns that is created by the propagation of the acoustic waves along the length of the support columns is not expected. The acoustic pressure wave varies between  $-p_o$  and  $+p_o$  in a distance equal to  $\frac{1}{2}$  of its wavelength. Because the height of the support columns is relatively short compared to this wavelength, the phase relationship between the fundamental mode shape of the column supports and the acoustic pressure wave does not exhibit adequate compatibility to impart a significant harmonic force to the support columns. The higher order modes of the support columns exhibit even less compatibility with this harmonic excitation force.

#### 4.5.1.1.6 Computation Fluid Dynamics Analysis of RPV Upper Internals

The primary fluid velocity and density throughout the RV upper internals is determined with a three dimensional CFD model for the full power normal operating condition. The CFD simulation represents the upper part of the U.S. EPR vessel as shown in Figure 4-72. Its computational domain is limited by the UCP, the USP, and the end of the hot legs. It is composed of:

- The UCP, with its orifices of three different types.
- The upper plenum, with its different elements.
- The outlet nozzles and the four hot legs, which are 10 diameters long (so that outlet conditions are far enough from the plenum).

Inside the plenum, the CRGAs, the first two guide plates as well as the lateral openings (toward the plenum volume) are modeled. The internal components of the CRGAs (tie rods, continuous guides, split tubes and rods) are not represented because they do not have any impact on the flow patterns around the columns. The vertical flow through the CRGA column support is blocked slightly above the second guide plate (in both the plant design and mock-up) as most of the flow goes outside, passing through the gussets. The LMP and Normal support columns have also been represented.

### Code Convergence

To demonstrate code convergence, five points are chosen in the computational domain:

- Three points located in the hot leg 3 near the scoop section.
- Two points located in the plenum between hot leg 3 and hot leg 4 (where there may be strong fluctuations).

The local velocity components (in m/s) as well as the temperature (in °K) are monitored during the iterations for each probe, and their evolutions are plotted. The convergence criteria are fixed at  $10^{-4}$  for the momentum equation and  $10^{-3}$  for the continuity equation, and are achieved at 6200 iterations.

### ROMEIO Test Details

The goal of the ROMEIO tests is to characterize the upper plenum hydraulics of the U.S. EPR RV internals. The ROMEIO mock-up represents the upper part of the EPR vessel at a scale of (1/5.2). The simulated part is located between the UCP, the USP, and the end of the hot legs.

The core effect is taken into account by additive head losses through the UCP. The CRGAs, columns, and aeroballs lance fingers are geometrically represented.

The UCP of the mock-up consists of two plates separated by 241 ventures (of which aim is to measure flow rates through the UCP). Each plate is drilled with 241 holes and diaphragms are inserted in the upstream holes. These diaphragms are of three types, CRGA, column, and free orifice, as there are three different outlet groups. The diameters of the diaphragms are determined to represent the upstream effect of the core on flow distribution. The methodology follows:

- Realization of a computation of the reactor upper plenum hydraulics with simulation of fuel assemblies, using porous media and singular head losses. The length of represented core is about one meter or 39.37 inches.

- Realization of a computation of the reactor upper plenum hydraulics with an empty core cavity upstream UCP (with representation of UCP holes, but without representation of fuel bundles).
- Determination of additive head loss coefficient to put into UCP holes in the empty cavity computation in order to obtain the same flow rate distribution with the simulation of fuel assemblies.

The mock-up is designed to obtain a uniform pressure distribution upstream the UCP. In this way, the UCP flow field is only created by downstream effects and in particular by the hot leg suction effect.

#### CFD Analysis Validation Procedure

The CFD analysis of the U.S. EPR upper internals is performed using the AREVA computer program "STAR-CD" Version 4.02. The results of the computer runs performed for the validation of STAR-CD are compared with analytical or semi-analytical solutions and also with measurements obtained from experiments where both the integral and separate effects are verified.

The validation includes the comparisons of the results obtained with the computations and experiments that are specifically dedicated to be representative of physical phenomena occurring in a pressurized reactor vessel. These experiments include U.S. EPR upper internals hydraulics, represented at scale 1/5.2 in ROMEO mock-up.

The CFD analysis does not include a sensitivity study of grid size; however, the accuracy of the model is demonstrated by the following methodology:

1. The model is validated with ROMEO mock-up, which is representative of the U.S. EPR upper internals geometry at ~one-fifth scale. This validation relies on comparisons of experimental and calculation results of:
  - The velocity fields in the hot legs (by means of Particle Interference Velocimetry (PIV)/ Laser Doppler Velocimetry (LDV) measurements).
  - The thermal mixing in the hot legs by means of temperature measurements.
  - The flow distribution in the upper plenum (by means of brine concentration measurements).
2. Other comparisons that are performed between the analytical solution and the test results that reinforce the validation of the CFD model are:
  - The pressure field over the upper support plate, which shows overpressure in the center of the plenum and under pressure near the hot legs, is very consistent between the numerical model and the tests and thus demonstrates a good prediction of the suction effect.
  - The hydraulic loads measured on CRGA column supports during steady state flow conditions are predicted very well by the numerical models.

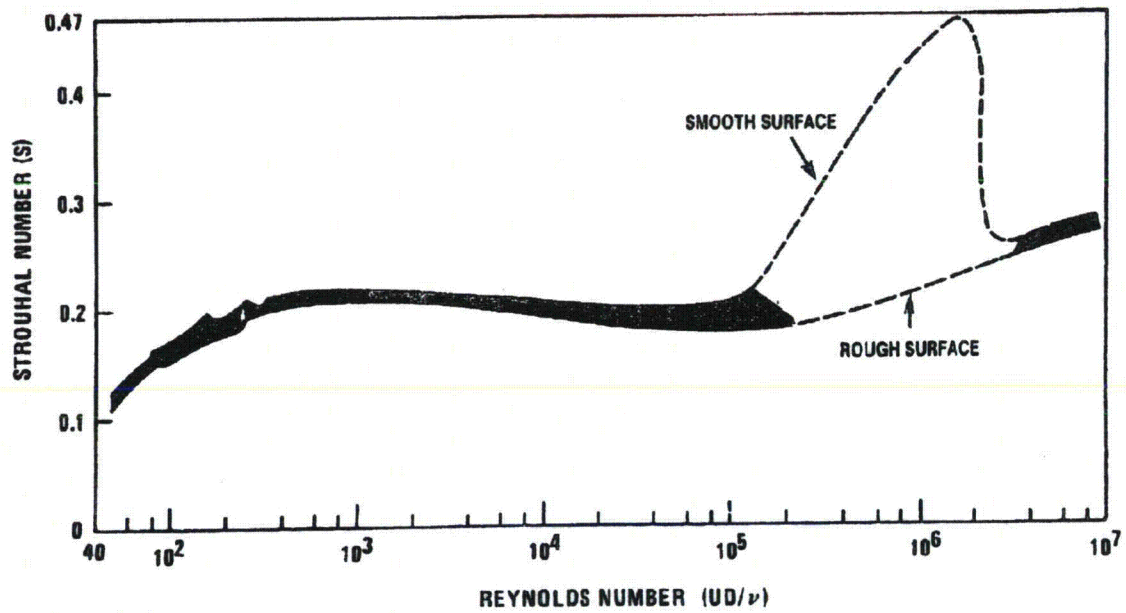
3. The similarity of the Reynolds number of the mock-up when compared to the numerical model validates the numerical model. This validation allows for the reliable numerical model at reactor scale.
4. The mesh is specifically refined for the study in hot legs 3 and 4 at reactor scale in order to assess a better calculation of the flow phenomenology in the hot legs which are under focus. Such a refinement increases the mesh size to 15.4 million cells which is sufficient to handle the mixing phenomenology in the upper plenum according to our engineering feedback.
5. Calculation at the wall boundaries is checked by post processing the  $y^+$  parameter in the computational domain (equivalent to a Reynolds number at wall). The recommended value is reached globally, which provides confidence in the validity of the standard functions, and subsequently, in the computational results.

The U.S. EPR upper plenum thermal hydraulic model is qualified based on benchmarking with flow tests performed with the ROMEO mock-up which simulates the upper internals at a scale of 1:5.2. The worst located column support is evaluated. As noted in Section 4.5.1, the cross flow velocity distribution along the length of the column supports is increased by 10 percent to account for the RCP over-speed transient conditions.

**Table 4-17—Modal Damping Ratio (%) for Column Supports  
 (Viscous)  
 (Used only for Vortex-Shedding Excitation)**

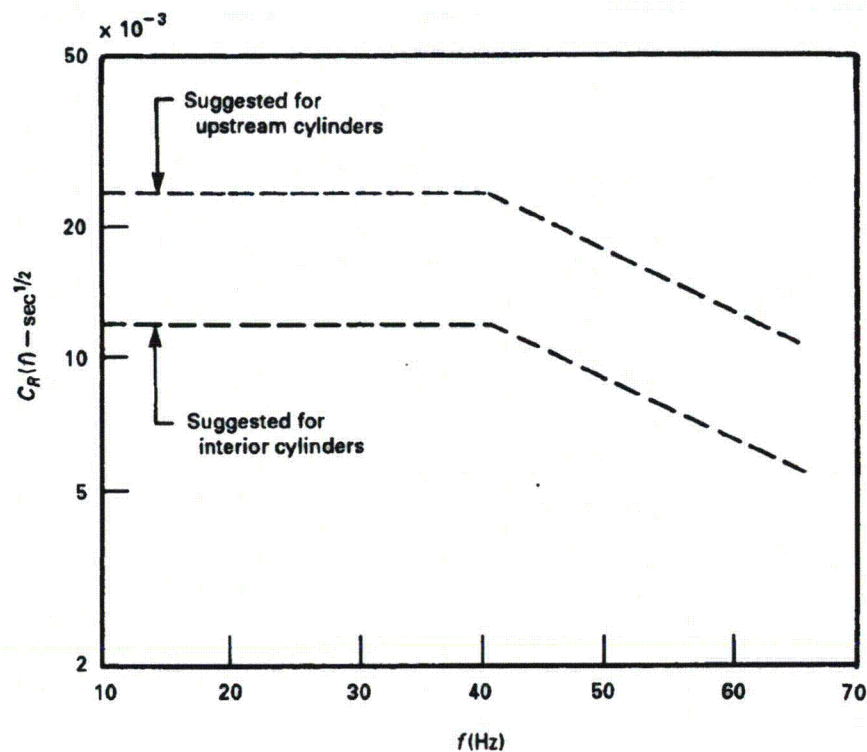


**Figure 4-33—Strouhal Number as a Function of Reynolds Number**



Notes for Figure 4-33:

1. Per Reference 2, Figure 3-3.

**Figure 4-34—Random Lift Coefficient for Arrays in Cross Flow**

Where:

$$C_R(f) = 10^{(af + b)}$$

$$= 0.025 \quad \text{for } f < 40 \text{ Hz.}$$

$$= 0.010 \quad \text{for } f = 65 \text{ Hz.}$$

where,

$$a = -15.92\text{E-}03, \quad b = -965.4\text{E-}03.$$

## 4.5.2 FIV Acceptance Criteria for the Column Supports

### 4.5.2.1 Fluid-elastic Instability

The FSM is the ratio of the critical velocity where an array of cylinders is predicted to become unstable to the equivalent mode shape weighted pitch velocity. An FSM greater than 1.0 implies that the array of cylinders is stable, while an FSM less than 1.0 implies that the array of cylinders will become unstable. For the U.S. EPR, a conservative acceptance criterion for fluid-elastic instability of FSM greater than 1.3 is used, which represents a margin of safety 30 percent.